RESEARCH ARTICLE SUMMARY

MOLECULAR BIOLOGY

CiBER-seq dissects genetic networks by quantitative CRISPRi profiling of expression phenotypes

Ryan Muller, Zuriah A. Meacham, Lucas Ferguson, Nicholas T. Ingolia*

INTRODUCTION: Systematically profiling the effects of genetic perturbations is a powerful approach that has revealed the molecular basis for a wide range of biological phenomena. The simple, programmable DNA recognition of CRISPR-Cas9 enables genome-wide genetic analysis in human cells and many other systems. Cas9 is guided by a short RNA to a complementary sequence in the genome, where it can introduce mutations or alter gene expression. Pooled libraries of guide RNAs (gRNAs) that individually target each gene in the genome allow us to introduce genetic perturbations systematically into a population of cells. A key challenge is measuring the phenotypic effects caused by individual guides in these pooled libraries and linking these phenotypes back to the associated gRNA, thereby finding the gene that is responsible.

RATIONALE: Molecular phenotypes such as gene expression changes provide a clear and sensitive measure for many cellular processes. We sought a general approach to profile how the expression of a particular gene of interest changed when other genes were perturbed.

We began with a library of gRNAs, each disrupting one gene, and linked these guides with an expression reporter containing a guide-specific nucleotide barcode. gRNAs that alter reporter expression will change the abundance of the expressed RNA barcode specifically associated with that guide. Deep sequencing of these expressed barcodes quantifies each of these guide-specific reporter expression effects individually within a pooled, complex population. We have implemented this strategy by combining CRISPR interference (CRISPRi) with barcoded expression reporter sequencing (CiBER-seq).

RESULTS: We used CiBER-seq to profile the responses of several yeast promoters tied to a range of biological functions. Each promoter yielded a distinct pattern of responses that could be understood in terms of its known function and regulation. For example, we rediscover the control of *MET6* expression by regulatory ubiquitylation and connect the bud scar protein Cwp1 to other genes required for budding and cytokinesis. Our analysis of the *HIS4* promoter, a well-characterized target of the integrated stress response, yielded a range of genetic perturbations that activate this pathway by causing the accumulation of uncharged transfer RNAs (tRNAs). We also uncovered a notable role for tRNA depletion in this response, as impaired tRNA biogenesis activated *HIS4* expression through a distinct pathway. In order to understand this regulation, we carried out genetic interaction analysis and looked for quantitative deviations in CiBER-seq profiles caused by the introduction of a second genetic perturbation. We also developed an indirect CiBER-seq approach to measure translational and posttranslational regulation, which both play roles in the signaling pathways upstream of *HIS4*.

CONCLUSION: CiBER-seq produces comprehensive phenotypic profiles that offer insights into gene function and regulation. These high-throughput and quantitative phenotypic measurements are also well suited for the systematic measurement of genetic interactions, which contain rich information about the operation of biological processes. This approach can be applied to study a wide range of transcriptional, translational, and posttranslational regulatory responses, and it has the potential to shed light on many areas of biology. ■
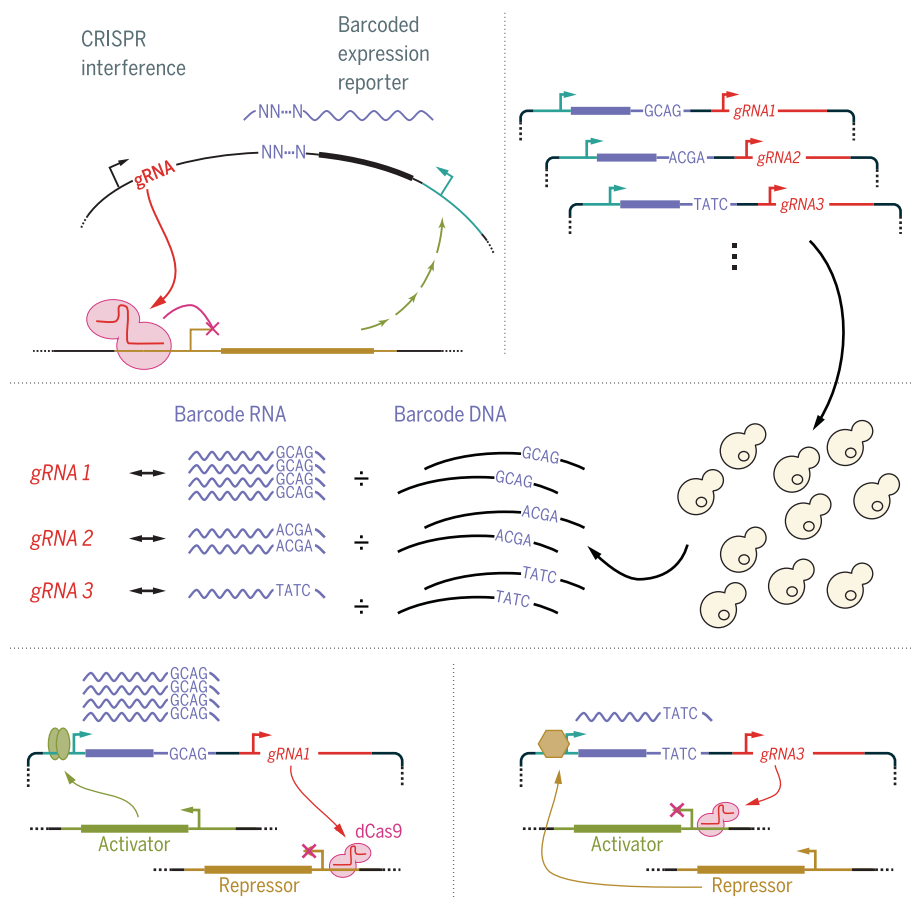
CRISPRi with barcoded expression reporters. CRISPR-Cas9 gRNA cassettes are linked with transcriptional reporters containing specific barcodes. The RNA-to-DNA ratio for each barcode, measured by deep sequencing, reveals the reporter expression phenotype induced by each gRNA.

READ THE FULL ARTICLE AT
https://doi.org/10.1126/science.abb9662

RESEARCH ARTICLE

MOLECULAR BIOLOGY

CiBER-seq dissects genetic networks by quantitative CRISPRi profiling of expression phenotypes

Ryan Muller[1], Zuriah A. Meacham[1], Lucas Ferguson[1], Nicholas T. Ingolia[1,2]*

To realize the promise of CRISPR-Cas9–based genetics, approaches are needed to quantify a specific, molecular phenotype across genome-wide libraries of genetic perturbations. We addressed this challenge by profiling transcriptional, translational, and posttranslational reporters using CRISPR interference (CRISPRi) with barcoded expression reporter sequencing (CiBER-seq). Our barcoding approach allowed us to connect an entire library of guides to their individual phenotypic consequences using pooled sequencing. CiBER-seq profiling fully recapitulated the integrated stress response (ISR) pathway in yeast. Genetic perturbations causing uncharged transfer RNA (tRNA) accumulation activated ISR reporter transcription. Notably, tRNA insufficiency also activated the reporter, independent of the uncharged tRNA sensor. By uncovering alternate triggers for ISR activation, we illustrate how precise, comprehensive CiBER-seq profiling provides a powerful and broadly applicable tool for dissecting genetic networks.

C RISPR-Cas9 has emerged as a powerful and versatile tool for creating precise, programmable genetic perturbations (*1*). CRISPR-based knockout (*2–4*) and knockdown (*5*) approaches enable systematic, genome-wide genetic analysis in a wide range of cells and organisms. The Cas9 protein binds short RNAs that guide this protein-RNA complex to complementary sites in the genome, where it can induce mutations or silence promoters (*1*). Libraries of guide RNAs (gRNAs), each targeting one individual gene, can be used to create a population of cells that each express one distinct guide (*6–8*). The phenotype of each cell then reflects the impact of the single guide that it expresses. It is straightforward to identify guides that affect cell survival or proliferation, but growth is a crude phenotype that is poorly suited to address many important biological questions (*9*). The scope of CRISPR-based genetics would be expanded by improved techniques to measure more-specific and relevant phenotypes across this diverse population and link these measurements back to individual guides.

Molecular phenotypes, such as the expression level of a critical gene or the stability of a key protein, provide a focused and sensitive gauge for many aspects of cell physiology. We devised an approach for profiling a transcriptional, translational, or posttranslational regulatory response comprehensively across CRISPR-based perturbations genome-wide. We adapted barcoded expression reporters (*10*) to produce quantitative phenotypic profiles from bulk sequencing of highly diverse populations. These profiles also enabled high-precision genetic interaction analyses, which use double-mutant phenotypes to map the structure of regulatory networks (*11*). This direct sequencing approach offers substantial advantages over fluorescent reporters for CRISPR-based genetics. Fluorescence phenotypes are typically analyzed by cell sorting (*9*), which imposes bottlenecks on the cell population size and discretizes quantitative fluorescence measurements into a few broad gates. Our approach circumvented both of these limitations. It also complemented broader expression profiles from single-cell approaches such as Perturb-seq (*12, 13*), CRISP-seq (*14*), and CROP-seq (*15*), which cannot currently capture enough cells to approach genome-scale coverage. Thus, better ways to profile molecular phenotypes across genome-scale guide libraries stand to benefit many areas of biology. Here, we combined CRISPR interference (CRISPRi) with barcoded expression reporter sequencing (CiBER-seq) to measure cellular responses provoked by gRNA-mediated knockdown.

Results

Barcoded expression reporters linked transcriptional responses with gRNA-mediated perturbations in massively parallel screens

The development of CiBER-seq relied on massively parallel measurements of reporter expression in a diverse population by the deep sequencing of short-sequence barcodes embedded in the reporter transcript (*10*). Each barcode was linked to one gRNA, and the RNA abundance of each barcode reflected reporter expression levels in the cells containing that barcode and expressing the associated guide (fig. S1). Barcode RNA levels are also affected by the variable abundance of cells containing the barcode and its associated guide and by nonspecific disruptions of cell viability or transcription. To correct for these confounding effects, we paired each barcoded reporter with a barcoded control transcript driven from a housekeeping promoter, which will experience the same overall cellular environment. We implemented CiBER-seq in budding yeast and delivered guide-reporter pairs on autonomous low-copy plasmids. We tagged each guide sequence in a comprehensive yeast gRNA library with pairs of random nucleotide barcodes and determined the linkage between barcode pairs and guides by long-read next-generation sequencing (Fig. 1A). Our library contained 10 guides per gene (~60,000 in total) (*16*) and ~240,000 distinct barcode pairs (approximately four per guide on average). By linking multiple barcodes with each guide, we were able to obtain independent measurements of guide effects in a single experiment.

We drove gRNA expression from a tetracycline-inducible promoter (*17*), which allowed us to specifically measure the difference in barcode expression before and after guide induction. This experimental design allowed us to exclude technical effects resulting from the sequence of a barcode. Inducible CRISPRi also facilitated the measurements of guides with strong fitness effects by allowing us to propagate cells without guide induction and thereby avoid the premature loss of guides with growth defects. We analyzed the multifactorial barcode abundance data in a generalized linear model framework, implemented by a massively parallel reporter assay linear model (mpralm) (*18*), which estimates the change in reporter expression caused by CRISPRi guide induction while controlling for baseline reporter expression and changes in the paired housekeeping barcode. This framework allowed us to incorporate replicate measurements, and we carried out all CiBER-seq experiments in biological duplicate. It also allowed us to identify guides causing a statistically significant change in normalized reporter expression, using statistical approaches developed for gene expression measurements in limma (linear models for microarray data) (*19*).

To explore whether CiBER-seq could dissect a range of regulatory circuits, we profiled the responses of four promoters—P(MET6), P(CWP1), P(PHO5), and P(HIS4)—whose gene products encompass a wide range of cellular roles. The protein product of MET6 catalyzes the conversion of homocysteine to L-methionine and plays a central role in sulfur and one-carbon metabolism. The activity of P(MET6) is controlled by the transcription factor Met4, which is ubiquitinated and inactivated by the SCF^MET30 complex (*20*) (Fig. 1B). In agreement with the inhibitory effect of SCF^MET30, CiBER-seq analysis of P(MET6) regulation identified several guides

[1]Department of Molecular and Cell Biology, University of California, Berkeley, Berkeley, CA 94720, USA. [2]California Institute for Quantitative Biosciences, University of California, Berkeley, Berkeley, CA 94720, USA.
*Corresponding author. Email: ingolia@berkeley.edu

Fig. 1. Barcoded expression reporters linked transcriptional responses with gRNA-mediated perturbations in massively parallel screens. (**A**) Schematic of CiBER-seq profiling experiment. Barcode expression is driven by a query promoter or matched P(PGK1) normalizer. Changes in relative barcode expression after gRNA induction link individual gRNAs with their corresponding phenotypic effect. (**B**) Model diagram of the SCF^MET30 complex. Subunits with at least one significant guide [q < 0.05 and >1.5-fold P(MET6) increase] are colored green. (**C**) Genome-wide CiBER-seq profile of P(MET6) transcription changes upon gRNA induction, relative to P(PGK1). Each point represents one gRNA, with guides against SCF^MET30 complex or MET6 itself colored as indicated. Lines indicate cutoffs for significant (q < 0.05) and substantial (>1.5-fold change) effects. (**D**) Genome-wide CiBER-seq profile of P(CWP1) transcription, as in (C), with guides against cytokinesis GO term genes and CWP1 itself colored as indicated. Significant guides against cyto-kinesis genes MLC1, CDC10, and CHS2 are labeled; the guide with the strongest q value was selected for validation. (**E**) Endogenous CWP1 mRNA measurements before and after MLC1, CDC10, and CHS2 knockdown. Error bars are the stan-dard deviation across N = 3 biological replicates. (**F**) GO analysis of each CiBER-seq query promoter profile. Guides were filtered by q < 0.05 and >2-fold increase, and resulting gene lists were analyzed for GO category overrepresentation using Fisher's exact test with false discovery rate (FDR)–adjusted P < 0.05. The most statistically significant entry was chosen from chains of hierarchically nested categories, and all chains with significant categories for any promoter are represented in the plot.
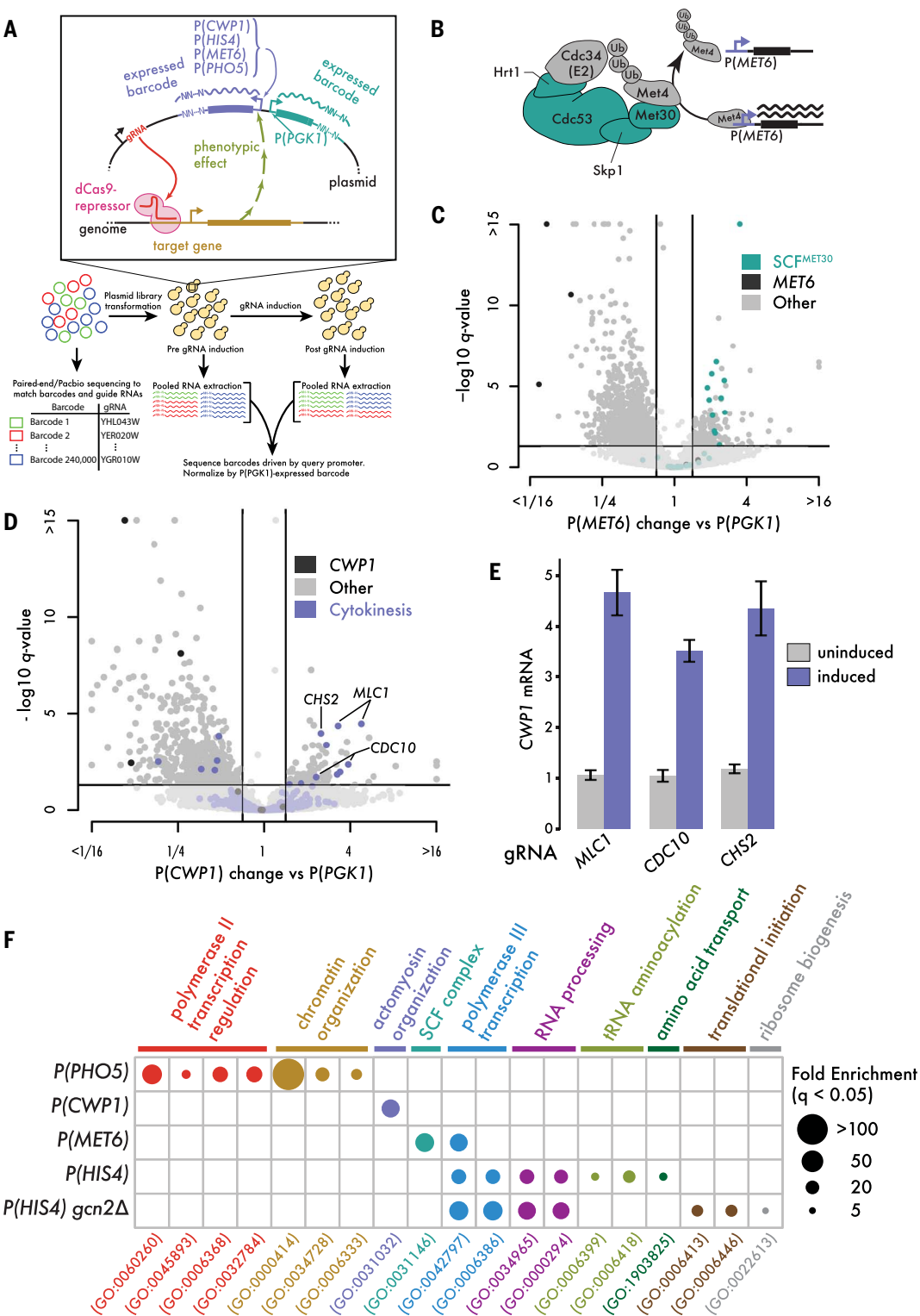
targeting this complex that increased P(MET6)-driven barcode expression relative to P(PGK1) controls (Fig. 1, B and C, fig. S2A, and data S1). We found a 32-fold enrichment (q < 1.3 × 10^{−5}) for this functional category among guides activating P(MET6), spanning nearly every sub-unit of this complex.

CiBER-seq analysis indicated that P(CWP1) activity was increased by genetic perturbation of cytokinesis. The Cwp1 protein localizes to bud scars, the cell wall structures formed at the site of cytokinesis in budding yeast (21). Appropriately regulated transcription of CWP1 is important for this localization, although the

mode of its regulation is unknown. We found that gRNAs targeting genes involved in budding and cytokinesis—including septins, myosin, and chitin synthase (22)—all activated P(CWP1) (Fig. 1D and data S1). We validated that knockdown of three representative genes, MLC1, CDC10, and CHS2, all induced the endogenous CWP1 gene

(Fig. 1E). Thus, P(*CWP1*) is activated by a coherent set of gRNAs that is consistent with the link between Cwp1 and budding.

Each of the four promoters displayed a distinctive and largely nonoverlapping phenotypic profile consistent with their known regulation and function (Fig. 1F and tables S1 to S4). CiBER-seq profiling of P(*PHO5*), a model promoter for early studies of chromatin-based transcription regulation (*23*), identified a collection of genes involved in nucleosome remodeling and RNA polymerase II initiation (fig. S2B and data S1). Similarly, P(*HIS4*) CiBER-seq yielded a complex profile of responses, including activation of P(*HIS4*) by knockdown of aminoacyl-tRNA synthetases (fig. S2C and data S1). The *HIS4* gene, which encodes an amino acid biosynthetic enzyme, is a well-characterized transcriptional target of the yeast integrated stress response (ISR), also known as the general amino acid control (GAAC) response. This deeply conserved pathway up-regulates biosynthetic genes in response to elevated levels of uncharged tRNAs that arise during amino acid starvation (*24*). It is therefore easy to understand how directly impairing tRNA charging by knockdown of the synthetase enzyme that carries out this reaction would trigger the ISR and thereby activate P(*HIS4*) as well as P(*MET6*), which is also an ISR transcriptional target.

We also observed clear P(*HIS4*) and P(*MET6*) activation from guides targeting RNA polymerase III, a scenario that should result in the absence of tRNA rather than the accumulation of uncharged tRNA. Because these uncharged tRNAs are sensed by the Gcn2 kinase, we investigated how the CiBER-seq profile of P(*HIS4*) would differ in a gcn2Δ knockout strain. Deletion of this sensor kinase eliminated the response of P(*HIS4*) to guides against tRNA synthetases, whereas the effects of RNA polymerase III knockdown remained at least as strong (Fig. 1F, fig. S2D, and data S1). Because we did not observe any effect of these guides on P(*PHO5*) or P(*CWP1*), it seemed unlikely that our results reflected a change in the activity of the P(*PGK1*) promoter that we used as a common point of reference in these experiments. Nonetheless, we set out to profile P(*HIS4*) activity more directly, normalizing the RNA expression level of the barcode against the DNA abundance rather than a control promoter.

CiBER-seq recapitulated known genetic regulators of ISR and identified regulators related to tRNA insufficiency

CiBER-seq profiling of P(*HIS4*) and P(*PGK1*) individually, with normalization against barcode DNA abundance (Fig. 2A and fig. S3), allowed us to unambiguously attribute observed transcriptional responses to one promoter. Our unbiased gene ontology (GO) analysis captured specific and distinct categories of P(*PGK1*) and

P(*HIS4*) activators (Fig. 2B and tables S6 and S7), in agreement with a direct comparison of P(*HIS4*) and P(*PGK1*) effects during CRISPRi perturbation (Fig. 2A and fig. S3, A and B). Although guides that activated P(*HIS4*) did not induce P(*PGK1*), knockdown of general RNA polymerase II transcription reduced expression in both reporters (fig. S3, A to E). Additionally, analysis of P(*PGK1*) in isolation demonstrated a clear induction in response
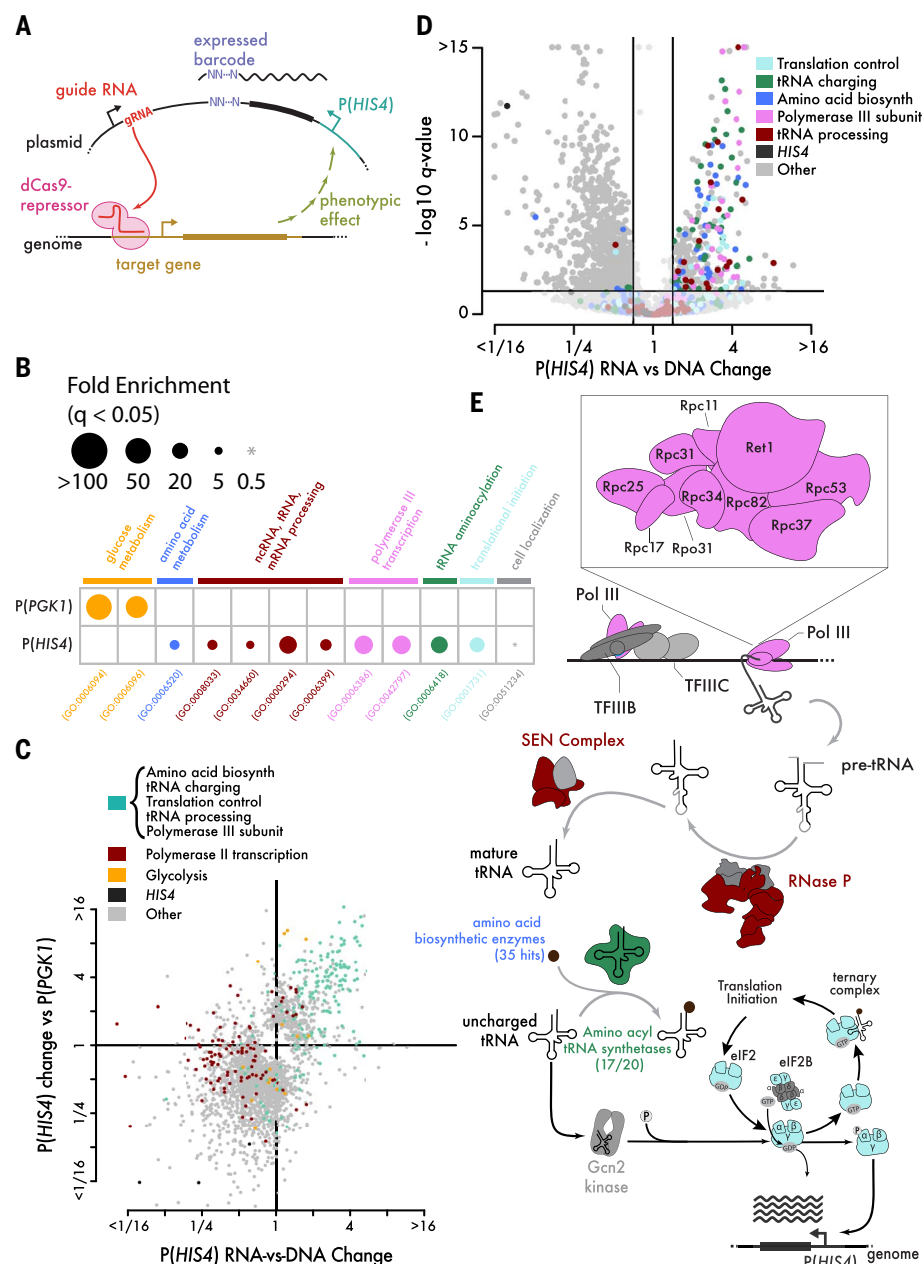

Fig. 2. CiBER-seq recapitulated known genetic regulators of ISR and identified regulators related to tRNA insufficiency. (**A**) Schematic of CiBER-seq profiling experiment, with modifications to isolate the regulatory effects of guide-mediated knockdown on a single promoter. (**B**) GO analysis of P(*PGK1*) and P(*HIS4*) with DNA normalization, as in Fig. 1F. (**C**) Comparison of CiBER-seq profiles for P(*PGK1*)–normalized and DNA-normalized P(*HIS4*) CiBER-seq analysis. Guides with significant effects in either profile are shown, and all GO terms highlighted in (B) are condensed to one group. (**D**) Genome-wide CiBER-seq profile of P(*HIS4*) transcription relative to DNA barcode abundance. Each point represents a different gRNA, analyzed to determine the change in P(*HIS4*) barcode RNA levels upon gRNA induction, normalized against the change in barcode DNA. The lines indicate cutoffs for significant (*q* < 0.05) and substantial (>1.5-fold change) effects. Guides are color coded by relevant statistically overrepresented GO terms with strong effects on P(*HIS4*). (**E**) Schematic of biological complexes with significant guides [as in (D)], with colors corresponding to GO terms. Subunits without a significant guide are displayed in gray. Pol III, polymerase III; TFIII, transcription factor for Pol III.
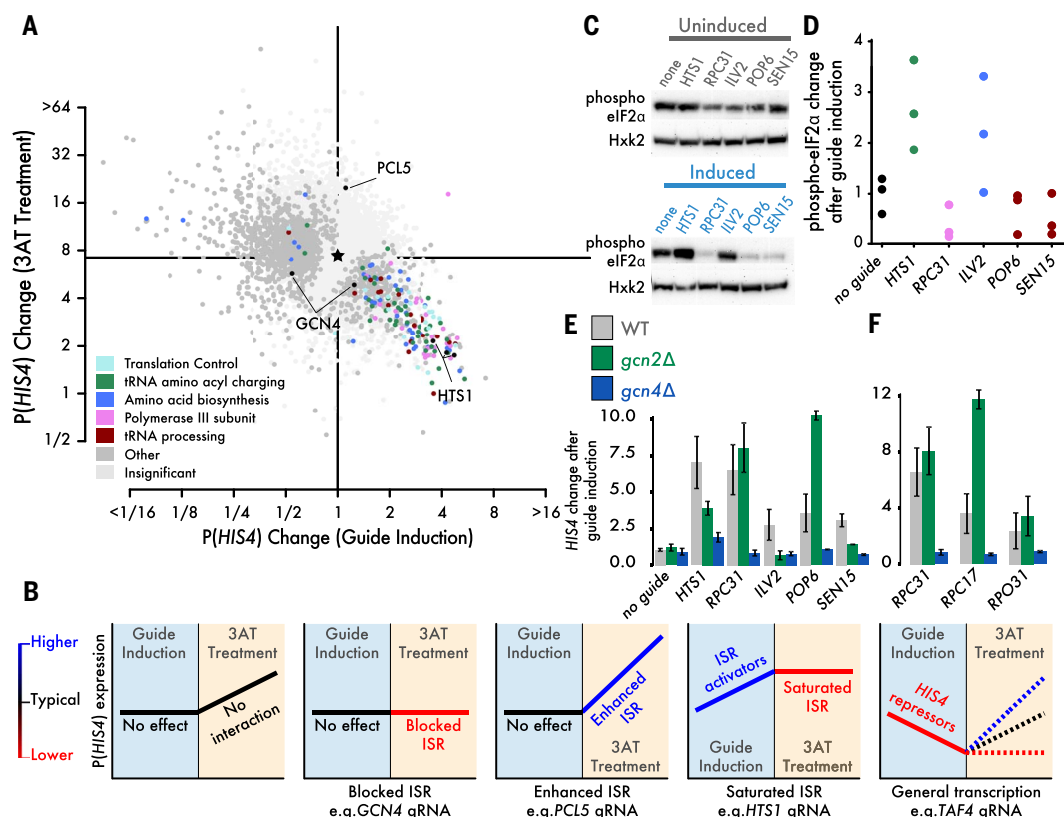
Fig. 3. tRNA insufficiency triggered HIS4 transcription independently of eIF2α phosphorylation and Gcn2 kinase. (**A**) Comparison of P(HIS4) CiBER-seq profiles before and after 3AT treatment, analyzed and colored as in Fig. 2D. (**B**) Schematic outlining expected ISR responses for CRISPRi knockdown of genes in various functional categories, before and after 3AT treatment. (**C**) Western blot for eIF2α phosphorylation relative to hexokinase (Hxk2) loading control. Knockdown of amino acid biosynthesis (ILV2) and aminoacyl tRNA charging (HTS1) increases eIF2α phosphorylation, whereas knockdown of RNA polymerase III (RPC31) or tRNA processing (POP6 and SEN15) does not. (**D**) Quantification of eIF2α phosphorylation relative to hexokinase loading control across N = 3 biological replicates. (**E**) Change in endogenous HIS4 mRNA levels after guide induction measured by qPCR. Endogenous HIS4 activation by ILV2, HTS1, RPC31, POP6, and SEN15 knockdown is completely GCN4 dependent. HIS4 activation by ILV2 knockdown is also completely GCN2 dependent, whereas effects of RPC31 and POP6 knockdown are entirely GCN2 independent, and HTS1 and SEN15 show intermediate dependency. Error bars represent standard deviation for N = 3 biological replicates. (**F**) As in (E) for guides targeting three distinct RNA polymerase III subunits. Error bars represent standard deviation for N = 3 biological replicates.

to knockdown of glycolytic enzymes (fig. S3, A to C), which suggests a homeostatic transcriptional activation of PGK1 expression in response to impaired glycolysis. Although the P(PGK1) promoter is often used with the intent to produce constitutive expression, it is subject to regulation (25), and Pgk1 activity increases when glycolysis is inhibited (26).

Our P(HIS4) CiBER-seq profile with DNA normalization confirmed observations from a previous profile based on P(PGK1) normalization—namely, that well-characterized defects in tRNA charging and newly identified deficiencies in tRNA synthesis affected P(HIS4) specifically (Fig. 2C). We thus surveyed the molecular complexes whose knockdown activated P(HIS4) (Fig. 2D). We identified 35 different gRNAs targeting amino acid biosynthesis pathways, along with guides against 17 of the 20 of the aminoacyl-tRNA synthetases (Fig. 2, D and E), which are all expected to interfere with tRNA charging. We also observed P(HIS4) activation

in response to knockdown of each individual component of the eIF2 translation initiation complex (Fig. 2, D and E); depletion of these proteins directly increases translation of the Gcn4 transcription factor, leading to P(HIS4) induction (24, 27).

We also found P(HIS4) activation in response to guides targeting many steps of tRNA biogenesis, which suggests that overall tRNA depletion triggered the ISR transcriptional program. Guides targeting subunits of RNA polymerase III, which transcribes tRNAs, as well as the tRNA processing complex ribonuclease (RNAse) P and the tRNA splicing endonuclease (SEN) complex (28) all activated P(HIS4) transcription (Fig. 2, A and C). In contrast to known ISR triggers, these genetic perturbations should not lead to the accumulation of uncharged tRNAs but should reduce overall tRNA levels. Although depletion of initiator methionyl-tRNA can induce P(HIS4) (29) and RNA polymerase III defects can lead to initiator methionyl-tRNA

depletion (30), this effect could not explain our observations here. Initiator tRNA does not contain an intron, and so the loss of SEN should not reduce initiator tRNA levels. To further exclude initiator tRNA depletion as an explanation for the effects of RNA polymerase III knockdown, we overexpressed initiator tRNA during CRISPRi-mediated ISR activation (fig. S3, J and K). Impaired tRNA transcription showed no particular susceptibility to suppression of the ISR response by high-copy overexpression of initiator tRNA, relative to disruption of amino acid biosynthesis or tRNA charging (fig. S3K). Thus, elongator tRNA depletion can directly activate ISR transcription, perhaps through its effects on translation elongation.

tRNA insufficiency triggered HIS4 transcription independently of eIF2α phosphorylation and Gcn2 kinase

Because the ISR is not activated during log-phase growth, our initial CiBER-seq data did
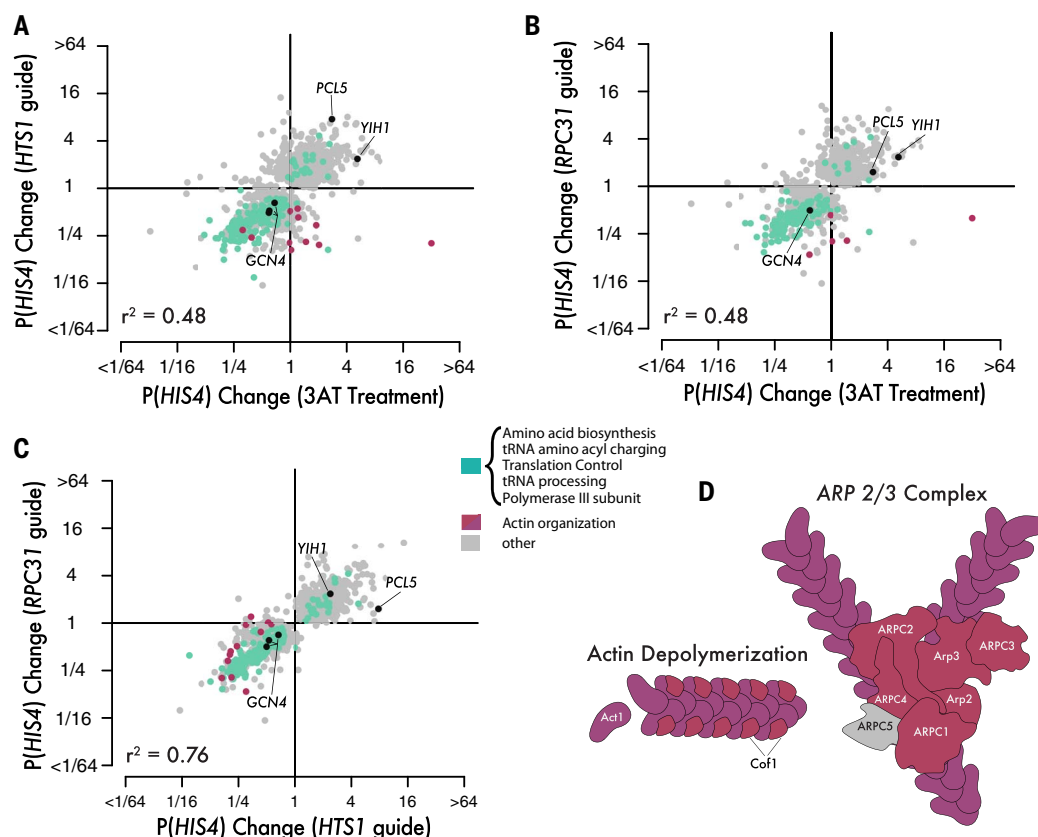
Fig. 4. Perturbations of the ARP2/3 complex prevented ISR activation by HTS1 or RPC31 knockdown. (A to C) Pair-wise comparison of P(HIS4) CiBER-seq profiles between ISR activation by 3AT treatment, HTS1 knockdown, and RPC31 knockdown. CiBER-seq profiles represent changes in the guide effect on P(HIS4) expression in the context of an ISR activator (as in Fig. 3A) relative to the change caused by the guide in isolation (as in Fig. 2D). Plotted guides were significant (q < 0.05) in at least one of the three epistatic profiles. All guides, regardless of significance, were used to calculate the pairwise Pearson correlations. (D) Coverage of actin cytoskeleton and ARP2/3 complex by guides that block ISR induction during HTS1 or RPC31 knockdown but not 3AT treatment.

not identify expression changes caused by loss of canonical, positive transducers of ISR signaling, such as GCN2 and GCN4. To uncover the phenotypes of these and other ISR pathway genes, we next looked for regulators whose depletion would block P(HIS4) activation triggered by the toxic histidine analog 3-amino-1,2,4-triazole (3AT), which blocks histidine biosynthesis (Fig. 3, A and B). Guides that activated P(HIS4) under replete nutrient conditions did not further elevate P(HIS4) expression upon 3AT treatment (Fig. 3A). We inferred that Gcn4-mediated activation is saturated under these conditions; however, knockdown of Gcn4 degradation factors, such as PCL5 (31), can enhance 3AT-mediated P(HIS4) induction. Meanwhile, guides that reduced P(HIS4) transcription, including guides targeting the core RNA polymerase II transcription machinery (fig. S2, A to C), did not interfere with P(HIS4) activation upon 3AT treatment. We therefore reasoned that guides affecting amino acid biosynthesis, as well as tRNA charging, transcription, and processing, each saturated P(HIS4) transcription through a shared, GCN4-dependent mechanism.

Because a hallmark of ISR activation is the phosphorylation of eIF2α, we investigated whether tRNA insufficiency provoked this response. Although CRISPRi knockdown of the amino acid biosynthetic enzyme ILV2 or the histidyl-tRNA synthetase HTS1 both induced eIF2α phosphorylation, knockdown of the RNA polymerase III subunit RPC31 or tRNA processing and maturation factors POP6 and SEN15 did not (Fig. 3, C and D, and fig. S4A), consistent with previous observations (30). Deletion of GCN2, the only known eIF2α kinase in yeast (32), completely blocked eIF2α phosphorylation in all conditions tested (fig. S4B). Activation of P(HIS4) in the absence of eIF2α phosphorylation further distinguished the response to tRNA depletion upon RPC31 knockdown and the classical ISR pathway.

We thus tested the genetic requirements for activation of endogenous HIS4 transcription in response to these CRISPRi-mediated perturbations. Deletion of GCN4 blocked HIS4 activation by RPC31, POP6, and SEN15 knockdown as well as ILV2 and HTS1 knockdown, and so the effects of tRNA insufficiency and defects in tRNA maturation reflected a GCN4-mediated ISR.

Furthermore, GCN2 deletion produced distinct effects across these five CRISPRi knockdowns (Fig. 3E). Deletion of GCN2 completely blocked HIS4 induction in response to ILV2 depletion, consistent with canonical models of ISR signaling (33). Although HTS1 knockdown triggered strong eIF2α phosphorylation, GCN2 deletion only partially abrogated its transcriptional effects; SEN15, which did not induce eIF2α phosphorylation, nonetheless showed a weakened response in the deletion as well. Finally, RPC31 and POP6 knockdowns induced HIS4 transcription independent of GCN2, as we expected on the basis of the lack of eIF2α phosphorylation and P(HIS4) CiBER-seq analysis in a gcn2 null background (figs. S2D and S4C). Epistatic characterization of additional RNA polymerase III subunits RPC17 and RPO31 confirmed that tRNA insufficiency broadly activated P(HIS4) by means of a GCN2-independent mechanism and that this was not a RPC31-specific effect (Fig. 3F). Thus, translation elongation defects arising from impaired tRNA recruitment directly triggered GCN4-mediated transcriptional responses. Knockdown of tRNA synthetases activated the ISR by this
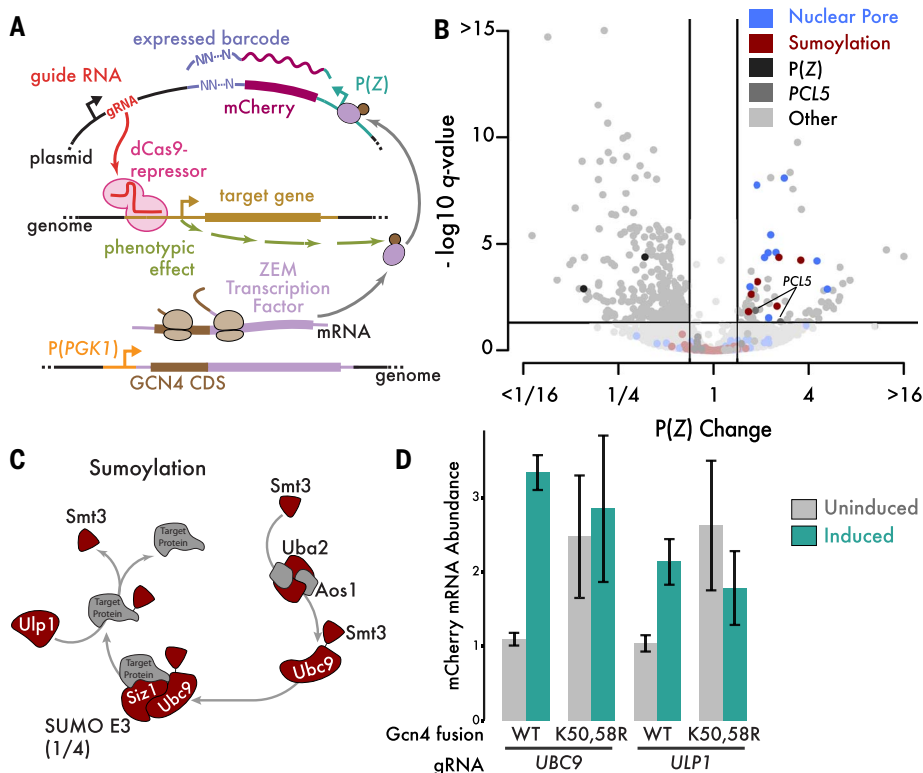
Fig. 5. Disrupting sumoylation enhanced the activity of Gcn4. (**A**) Schematic of indirect CiBER-seq experiment to identify posttranslational regulators of Gcn4. (**B**) CiBER-seq response of P(Z) driven by Gcn4-ZEM fusion, as in Fig. 2D. (**C**) Schematic of SUMOylation cycle. Proteins targeted by significant ($q < 0.05$ and >1.5-fold change) guides from (A) are colored, whereas proteins without a significant guide are gray. (**D**) Measurement of *mCherry* reporter mRNA abundance by qPCR in cells expressing the indicated Gcn4 fusion with the ZEM transcription factor and a gRNA targeting either *UBC9* or *ULP1*.

pathway in parallel with the *GCN2*-dependent response to uncharged tRNAs.

Perturbations of the ARP2/3 complex prevented ISR activation by HTS1 or RPC31 knockdown

Given the fact that both Gcn2 activity and eIF2α phosphorylation were dispensable for ISR activation in response to tRNA depletion, we next sought to systematically identify genes required for this response. We looked for genetic perturbations that modified P(HIS4) responses to different ISR triggers by performing dual-guide CiBER-seq—combining one guide that individually activated the ISR with a second guide from our genome-wide CRISPRi library to obtain quantitative, genome-wide genetic interaction profiles. We compared the interaction profiles of the histidyl-tRNA synthetase *HTS1*, which is required for tRNA charging, with those of the RNA polymerase III subunit *RPC31*, which is required for tRNA transcription (Fig. 4, A to C, and tables S8 and S9). We observed saturated P(HIS4) induction after knockdown of *HTS1* or *RPC31*, similar to the P(HIS4) saturation that we observed upon 3AT treatment (Fig. 3, A and B). Guides that activated the ISR on their own did not further enhance transcription in these dual-guide epis-

tasis experiments. We also observed guides that had no effect on their own but either suppressed ISR activation, such as guides against *GCN4* itself, or enhanced the strength of the response, including guides against the degradation factor *PCL5* or the ISR inhibitor *YIH1* (*34*, *35*).

We compared the genetic interaction profiles across three different ISR stimuli to test whether they were acting through similar or distinct pathways. Epistatic profiles of *HTS1* and *RPC31* knockdown resembled each other ($R^2 = 0.76$, where R^2 is the coefficient of determination) more closely than either of them resembled the profile during 3AT treatment ($R^2 = 0.48$), although all three profiles did overlap substantially. This pattern aligned with our observation that P(HIS4) activation by either tRNA charging defects or tRNA depletion were not completely *GCN2* dependent, whereas the amino acid starvation response was fully *GCN2* dependent (Fig. 3E). Thus, we looked for epistatic modifiers of P(HIS4) activation in response to *HTS1* and *RPC31* knockdown. Using unbiased GO enrichment analysis on the subset of observed guides that blocked ISR-mediated transcriptional activation (tables S8 and S9), we identified an unexpected requirement for the actin cytoskeletal components in this response

(Fig. 4). Although knockdown of actin itself (*ACT1*) or genes encoding members of the Arp2/3 complex (fold enrichment >14, $q < 0.002$ in both dual-guide datasets) did not affect P(HIS4) transcription in normal growth or 3AT treatment (fig. S5A), it blocked P(HIS4) activation by tRNA charging defects or tRNA depletion (fig. S5, B and C). This could reflect interactions between the ISR inhibitor *YIH1* and free actin monomers (*35*), or it could arise because of nuclear actin's role in transcription (*36*).

Disrupting sumoylation enhanced the activity of Gcn4

CiBER-seq analysis of P(HIS4) regulation provided a comprehensive view of yeast ISR signaling, which revealed distinct triggers for *GCN4*-dependent transcriptional responses. However, this approach did not allow us to distinguish the different layers of Gcn4 regulation. Gcn4 abundance is controlled by regulated protein degradation (*37*) in addition to its well-characterized translational induction upon eIF2α phosphorylation (*24*). We observed epistatic enhancement of ISR activation from guides depleting the decay factor *PCL5*. Thus, we wanted to specifically analyze the regulators of Gcn4 stability and translation in isolation and separate them from other effects on P(HIS4) activity. To couple these protein-level phenotypes with a transcriptional readout suitable for CiBER-seq, we returned to the synthetic, ZEM chimeric transcription factor used to initially validate barcode sequencing. Because barcode transcription was directly linked to the abundance of this synthetic transcription factor (fig. S1, E and I), we reasoned that it could couple protein-level regulation with expressed RNA barcode abundance (Fig. 5A).

We first profiled posttranslational control of Gcn4 by carrying out CiBER-seq in yeast that constitutively expressed a protein fusion between Gcn4 and the chimeric ZEM transcription factor (Fig. 5A and tables S10 and S11). Levels of this transcription factor should reflect only posttranslational regulation of Gcn4—and not its translational regulation—because it is expressed using the *PGK1* promoter and 5′ untranslated region (5′UTR). Knockdown of *PCL5*, which regulates Gcn4 degradation, affected the activity of the Gcn4-ZEM posttranslational reporter. However, neither tRNA charging nor tRNA biogenesis had an effect. Instead, disruption of sumoylation increased expression from P(Z) (Fig. 5, B and C). We identified individually significant gRNAs targeting nearly every step of the sumoylation pathway, including SUMO itself, SUMO-activating and SUMO-conjugating enzymes, and the Siz1 SUMO E3 ligase (*38*). Likewise, we identified guides against most components of the Nup84 subcomplex of the nuclear pore (*39*) that increased Gcn4-ZEM activity (Fig. 5B).
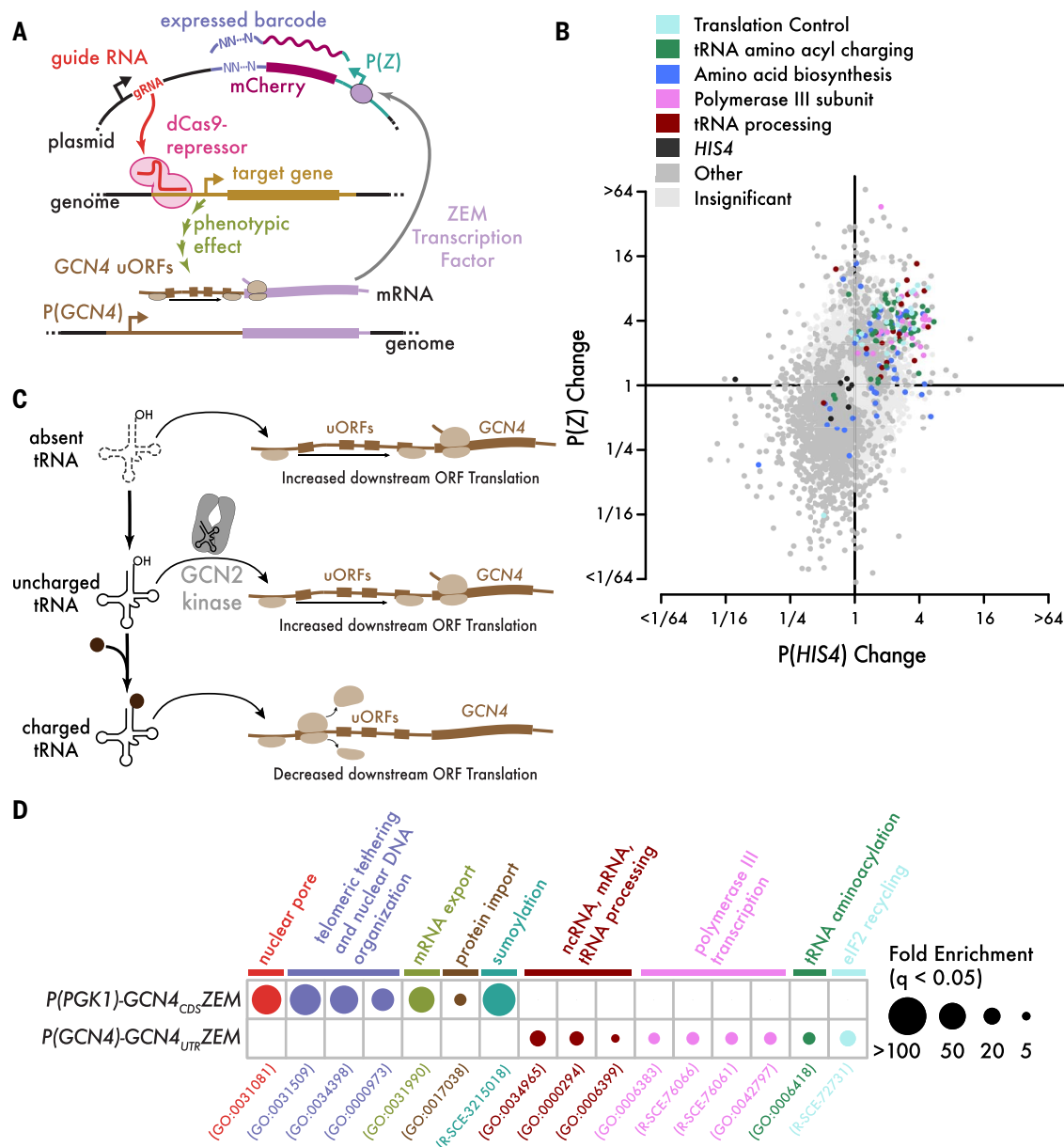
Fig. 6. The GCN4 5′ leader sequence is an intrinsic biosensor of translation stress. (**A**) Schematic of indirect CiBER-seq experiment to identify mediators of *GCN4* 5′ leader translation regulation. (**B**) Comparison of P(*HIS4*) DNA-normalized CiBER-seq profile (Fig. 2D) versus indirect P(*Z*) profile generated with P(*GCN4*)–UTR_GCN4–ZEM, with ISR activators colored according to their function, as in Fig. 2D. (**C**) Model of *GCN4* 5′ leader sequence as an intrinsic biosensor of translation stress. Either tRNA insufficiency or uncharged tRNAs increase *GCN4* translation. (**D**) GO analysis of indirect CiBER-seq experiments, as in Fig. 1F. Significant annotations were collected from both the GO biological process complete and reactome pathway annotation datasets. ORF, open reading frame.

Sumoylation of Gcn4 promotes its eviction from chromatin—even when it is recruited through heterologous DNA binding domains—and causes its subsequent degradation. Removal of Gcn4-ZEM from target promoters and degradation of the protein are both expected to limit transactivation of barcoded reporters (*40*, *41*), and knockdown of the SUMO conjugation machinery would relieve these limiting effects and enhance barcode expression. Elevated barcode expression during knockdown of the Ulp1 deconjugating protease could result from its role in SUMO maturation (*42*) or reflect

a more-complex requirement for a sumoylation-desumoylation cycle in Gcn4 regulation. Our Gcn4-ZEM fusion did retain the Gcn4 DNA binding domain, in addition to the heterologous Zif268 DNA binding domain, which could also contribute to the overall profile of responses that we observed.

The sites of SUMO modification on Gcn4 are known, and unSUMOylatable mutants have been reported. To directly test the role of SUMOylation in regulation of Gcn4p-mediated transcription, we generated a transcription factor fusion with the unSUMOylatable Gcn4

mutation (*40*) and measured its activity (Fig. 5D). The unSUMOylatable mutant caused higher baseline P(*Z*) expression that was not further increased upon SUMO cascade knockdown (Fig. 5D). Thus, Gcn4-specific SUMOylation is reducing the activity of the Gcn4-ZEM fusion, and this reduction is relieved when SUMOylation is impaired globally or blocked by Gcn4-specific mutations. The role of the nuclear pore, although less clear, may be linked to sumoylation. In yeast, Ulp1 binds physically to the nuclear pore (*43*, *44*), mutations in the Nup84 complex can mimic some *ulp1* phenotypes (*45*, *46*), and Ulp1 at the

nuclear pore has been implicated directly in transcriptional activation (*47*). Alternately, this effect may be specific to the Gcn4-ZEM fusion, although it did not arise in other CiBER-seq profiles based on the ZEM transcription factor, as described below.

The GCN4 5′ leader sequence is an intrinsic biosensor of translation stress

We observed clear and coherent patterns of genetic perturbation affecting Gcn4 protein activity, but we saw no evidence that tRNA insufficiency affected its posttranslational regulation. We next explored the translational control of *GCN4*, which results from regulatory upstream open reading frames in the *GCN4* 5′ leader sequence (*24*). To capture perturbations that affect this translation regulation, we drove expression of the ZEM synthetic transcription factor from the *GCN4* promoter and 5′ leader sequence and assessed guide effects on barcode expression (Fig. 6A).

The same guides that activated P(*HIS4*), including those that block tRNA biogenesis as well as tRNA charging, also increased P(*Z*) in our CiBER-seq analysis of translational control through the *GCN4* 5′ leader (>32-fold, hypergeometric $P < 2.04 \times 10^{-156}$) (Fig. 6B, fig. S6A, and tables S12 and S13). By assessing this translational response in isolation, we observed that effects occur in the same direction but with larger magnitude than P(*HIS4*). Thus, translational regulation is central to ISR activation, even when it proceeds independently of *GCN2* and eIF2α phosphorylation (Fig. 6C). To exclude transcriptional effects mediated by the *GCN4* promoter (*48*), we repeated this CiBER-seq profiling experiment with a version of the ZEM transcription factor driven from the P(*PGK1*) promoter, but still containing the *GCN4* 5′ leader (fig. S6B). This profile enriched most of the same functional categories as the profile using the *HIS4* promoter, including tRNA transcription and processing (fig. S6C). We observed an overall enrichment of shared activators between the two profiles (>11-fold, hypergeometric $P < 1.62 \times 10^{-61}$) and specific enrichment in tRNA biogenesis factors (>100-fold, hypergeometric $P < 8.88 \times 10^{-59}$).

Discussion

By linking CRISPRi guides with barcoded expression reporters, we generated quantitative, genome-wide phenotypic profiles for specific molecular events in the yeast cell. Our CiBER-seq approach allowed us to address transcriptional, translational, and posttranslational regulation, enabling the systematic genetic analysis of diverse biological processes. We characterized distinctive CiBER-seq profiles for five different promoters, each of which could be understood in light of the function of the associated gene. We leveraged these quantitative phenotypic profiles to gain insights

into the ISR, identifying tRNA depletion as a previously unappreciated trigger for this well-characterized pathway.

Because translation is a resource-intensive biosynthetic process, most organisms sense translational stresses and respond with physiological changes that maintain homeostasis. In eukaryotes, amino acid starvation, which directly affects tRNA charging and translation elongation, triggers a global decrease in translation initiation while also increasing the transcription of amino acid biosynthesis genes (*24*). In many cases, reduced initiation is sufficient to restore normal elongation profiles (*49*). In fact, when aminoacyl-tRNA synthetases are depleted, yeast reduces translation initiation until tRNA charging and utilization are balanced. Furthermore, in normal circumstances, these synthetases appear to buffer tRNA levels by sequestering uncharged tRNAs (*50*). Here, we found that the opposite situation—tRNA depletion in the presence of adequate synthetases and amino acids—triggered a *GCN2*-independent ISR. Our comprehensive genetic data, implicating many stages of tRNA biogenesis, suggest that *GCN4* translation responds directly to elongator tRNA insufficiency, rather than to depletion of initiator tRNA (*30*) or the accumulation of unprocessed nuclear tRNA precursors (*51*). Because we have not identified other trans-acting regulatory pathways under these circumstances, we propose that the *GCN4* 5′ leader is an intrinsic biosensor for translation elongation stress (Fig. 6C). Artificial stimuli, including tRNA depletion, can activate *GCN4* translation independent of eIF2α phosphorylation. In the natural history of budding yeast, the ISR likely evolved to sense nitrogen starvation and elicit general inhibition of translation through *GCN2*, along with *GCN4*-dependent activation of homeostatic transcriptional programs (*24*). Our work expands the range of stresses known to activate the ISR and points to a general mechanism for sensing translational perturbations.

Although we showed that the ISR is activated by artificial, genetic depletion of tRNAs, similar situations may arise in a natural context (*52*). Starvation and other stresses can induce tRNA cleavage (*53*, *54*), and although much attention has focused on the positive roles of the resulting fragments (*55*), cleavage can also deplete the tRNA substrate and alter translation (*56*). Effective tRNA depletion may also arise when tRNAs are sequestered in the nucleus and thus unavailable for cytosolic translation (*28*). Finally, an array of human disease mutations that affect tRNA biogenesis factors lead to neurodegenerative disorders, although the molecular basis for this effect is not clear (*52*, *57*). Mutations in tRNA genes themselves can lead to tRNA insufficiency, ISR activation, and neurodegeneration, although in mammals this effect is *GCN2* dependent (*58*, *59*).

Our results demonstrate the power of CiBER-seq in elucidating the genetic architecture of regulation in the cell. We observed distinct patterns of response for different promoters and comprehensive coverage of pathways and molecular complexes by guides targeting each individual component, which indicate that our approach is both specific and sensitive. We identified ISR activation upon knockdown of each subunit of RNA polymerase III along with most proteins involved in tRNA processing, which reveals tRNA depletion as the underlying trigger for the ISR. We identified other modes of regulation as well, such as sumoylation of Gcn4, and even detected the compensatory P(*PGK1*) activation in response to impaired glycolysis. Quantitative CiBER-seq profiles enable genetic interaction analysis that provides further insight into regulatory networks. Correlated patterns of epistasis are a powerful tool for identifying genes that function together in pathways and complexes, and likewise chemogenomic comparison between chemical and genetic interaction profiles can reveal functional drug targets (*11*). Here, we leveraged this advantage of CiBER-seq to identify a role for actin cytoskeletal components in ISR signaling. More broadly, our results highlight the power of CiBER-seq to combine specific and quantitative molecular phenotypes with targeted genetic perturbations and thereby precisely dissect regulatory pathways. A similar Reporter-seq technique has been developed simultaneously with this work, and it has been applied to elucidate known and unknown pathways linking diverse stressors to the yeast heat shock response (*60*). Because the key components of CiBER-seq translate into nearly any organism, we anticipate many biological insights will arise from broad application of our approach.

Materials and methods
Plasmid materials

pRS416-dCas9-Mxi1 + TetR + pRPR1(TetO)-NotI-gRNA was a gift from R. Davis (Addgene plasmid #73796; http://addgene.org/73796; RRID: Addgene_73796). pKT0139 was a gift from K. Thorn (Addgene plasmid #8731; http://addgene.org/8731; RRID: Addgene_8731). pHES836 was a gift from H. El-Samad (Addgene plasmid #89195; http://addgene.org/89195; RRID: Addgene_89195). pHES795 was a gift from H. El-Samad (Addgene plasmid #87943; http://addgene.org/87943; RRID: Addgene_87943). pCfB2337 was a gift from I. Borodina (Addgene plasmid #67555; http://addgene.org/67555; RRID: Addgene_67555). pCfB2226 was a gift from I. Borodina (Addgene plasmid #67533; http://addgene.org/67533; RRID: Addgene_67533). pCfB2189 was a gift from I. Borodina (Addgene plasmid #67532; http://addgene.org/67532; RRID: Addgene_67532). Plasmids used in this study are listed in table S1.

Plasmid construction

Oligonucleotides used in this study are listed in table S2. Plasmid assembly was carried out using standard molecular biology techniques as described below, and verified by Sanger sequencing. All polymerase chain reaction (PCR) reactions were performed using Q5 polymerase (NEB M0491S) according to manufacturer protocols. Restriction enzymes were obtained from NEB and high-fidelity (HF) variants were used when available. DNA fragments were size-selected by gel electrophoresis in 1% agarose. Gibson assembly reactions were carried out using NEBuilder HiFi DNA Assembly Master Mix (NEB E2621L) with DNA fragments containing homology arms between 15 and 20 base pairs (bp) long. DNA was purified and concentrated as necessary with DNA Clean & Concentrator (Zymo D4013). Transformations were performed in Stbl3 chemically competent cells provided by the QB3 Berkeley Macrolab facility and plated on appropriate antibiotic plates for colony selection. Plasmid DNA was purified from liquid cultures using DNA miniprep kit (NEB #T1010).

pNTI660 was constructed in several steps. First, pNTI601 (pRS416-dCas9-Mxi1 + TetR + pRPR1(TetO)-NotI-gRNA, AddGene #73796) (17) was amplified with NM717 and NM724 (16) to isolate the gRNA expression cassette and the resulting PCR product was recircularized by Gibson assembly to create pNTI646. pNTI646 was then digested with MfeI and combined with oligonucleotide NI1025 to create pNTI660.

pNTI725 was created in several steps. First, the promoter P(PGK1) was amplified from *Saccharomyces cerevisiae* BY4741 genomic DNA using NI553 and NI554, and the resulting product was subcloned and used as a template for P(PGK1) amplification. Yeast-optimized yECitrine coding sequence was amplified from pNTI189 (pKT0139 AddGene #8731) (61) using primers RM151 and RM155 and cloned downstream of P(PGK1). Next, the P(PGK1)-yECitrine expression fragment was isolated by digestion with SacI and BsrgI restriction sites, and pNTI660 was linearized by digestion with MfeI. Double-stranded DNA splints were created by annealing oligonucleotides RM317 and RM318 and oligonucleotides RM319 and RM320. Digested P(PGK1)-yECitrine and pNTI660 were joined together using these splints in a four-piece Gibson assembly reaction. The NotI site for gRNA insertion was replaced with an NruI site by digesting the backbone with NotI and then introducing single-stranded oligonucleotide RM321 by Gibson assembly. Finally, the Illumina TruSeq Read1 site was added to the beginning of the terminator T(ADH1) by annealing single-stranded oligonucleotides RM323 and RM324, extending them using Q5 polymerase, digesting the backbone with AscI and introducing the double-stranded product into the digested plasmid by Gibson assembly.

pNTI726 was constructed by replacing P(PGK1) in pNTI725 with estradiol-responsive P(GAL1). P(GAL1) with an embedded Zif268 binding site was PCR amplified from pHES836 using primers RM348 and RM349. pNTI725 was digested with SacI and EcoRI and amplified P(GAL1) was then Gibson assembled into the backbone.

pNTI727 was generated by inserting the gRNA sequence targeting P(Z) into pNTI726. Plasmid pNTI726 was digested with NruI, single-stranded oligonucleotides RM389 and RM390 were annealed, extended using Q5 DNA polymerase, and the double-stranded product was introduced into the linearized plasmid by Gibson assembly.

pNTI728 was generated by inserting the gRNA sequence targeting P(ADH1) into pNTI726, using the same methods as pNTI727, using oligonucleotides RM383 and RM384.

pNTI729 was constructed by first amplifying the ZEM transcription factor from pNTI638 (pHES795 Addgene #87943) (62) in two pieces, using oligonucleotide primers RM352 with RM353 and RM354 with RM355. The easy clone vector pCfB2337 (Addgene #67555) (63) was then digested with HindIII and the three fragments were combined by Gibson assembly.

pNTI730 was constructed by replacing the promoter P(ADH1) in pNTI729 with the P(PGK1) promoter. pNTI729 was digested with PvuII and NheI, P(PGK1) was amplified from pNTI725 using primers RM417 and RM418, and the two fragments were combined by Gibson assembly.

pNTI731 through pNTI737, expressing gRNAs against *ILV2*, *HTS1*, *RPC31*, *NUP133*, *NUP145*, *ULP1*, and *UBC9*, respectively, were subcloned into the integrating plasmid pCfB2189. First, DNA fragments containing the gRNA expression cassette were amplified from the pool of gRNA plasmids using forward primers RM639, RM517, RM518, and RM641 through 644, respectively, that anneal to the specific nucleotide barcode sequence, and a reverse primer RM519 that binds downstream of the gRNA scaffold. Fragments were amplified with Gibson homology arms on each end. The integration vector pCfB2189 (Addgene #67532) (63) was digested with HindIII and gRNA-expressing fragments were transferred into this backbone by Gibson assembly.

pNTI738 for initiator methionyl-tRNA overexpression was constructed by amplifying the initiator methionyl-tRNA locus *IMT4* from yeast genomic DNA using primers RM636 and RM637, digesting the high-copy yeast plasmid pRS426 (ATCC #77107) (64) with EcoRI, and combining them by Gibson assembly.

pNTI739 was constructed from pNTI730. The *GCN4* coding sequence (CDS) was amplified from yeast genomic DNA using primers RM515 and RM516 and inserted upstream of, and in frame with, the synthetic transcription factor by digesting pNTI730 with NheI and introducing *GCN4* by Gibson assembly.

pNTI740 was constructed by digesting NTI730 with PvuII and NheI, amplifying the *GCN4* promoter and 5′UTR from yeast genomic DNA using primers RM513 and RM514, and combining the two fragments by Gibson assembly.

pNTI741, the P(HIS4)-yECitrine PCR template used for downstream CiBER-seq plasmid library preparation, was generated by replacing the P(PGK1) in pNTI725 with P(HIS4). pNTI725 was digested with SacI and NheI, P(HIS4) was amplified from yeast genomic DNA using primers RM499 and RM500, and the two fragments were combined by Gibson assembly.

pNTI742 was made in several steps. First, the NotI restriction site of pNTI660 was replaced with an AvrII restriction site by digesting with NotI and introducing a replacement cassette, composed of annealed oligonucleotides RM459 and RM460, by Gibson assembly. Next, the vector was digested with SacI and MfeI. The T(ADH1) terminator and TruSeq Read1 priming site were amplified from pNTI726 using primers RM489, RM490, and RM491, in a nested PCR approach where RM490 was used at 0.1 times the normal concentration. The resulting PCR product was joined with the digested vector by Gibson assembly.

pNTI743 was made in several steps. First, the yeast *ACT1* 3′UTR and transcription termination sequence was PCR amplified from yeast genomic DNA using RM633 and RM634. pNTI742 was linearized with BamHI and the amplified PCR product was inserted by Gibson assembly. This intermediate vector was then digested with HindIII and AflII, and oligo RM719 was inserted by Gibson assembly.

pNTI744 through pNTI750, expressing gRNAs against *POP6*, *SEN15*, *RPC17*, *RPO31*, *MLC1*, *CDC10*, and *CHS2*, respectively, were subcloned into the integrating plasmid pCfB2189. First, DNA fragments containing the gRNA expression cassette were amplified from the pool of gRNA plasmids using forward primers RM722-725, RM813, RM814, and RM817, respectively, that anneal to the specific nucleotide barcode sequence, and a reverse primer RM519 that binds downstream of the gRNA scaffold. Fragments were amplified with Gibson homology arms on each end. The integration vector pCfB2189 (Addgene #67532) (63) was digested with HindIII and gRNA-expressing fragments were transferred into this backbone by Gibson assembly.

pNTI751 was constructed by three-piece Gibson of the following DNA fragments. First, P(PGK1) was PCR amplified from pNTI725 using primers RM726 and RM727. Second, the GCN4 5′UTR was amplified from pNTI740 using primers RM728 and RM729. Third, pNTI740 was digested with PvuII and HindIII and the 8600-bp fragment was gel extracted.

pNTI752 was constructed by first digesting pNTI739 with NheI and SapI, and gel extracting the 10-kb fragment. The K50,58R mutation was introduced into the GCN4 CDS by PCR amplifying the CDS from pNTI739 using primers RM730, RM731, and RM732 (731 was used at 0.1 times the concentration of the other two). pNTI752 was then assembled by three-piece Gibson of the linearized backbone, PCR fragment, and RM733 splint oligo.

pNTI753 was constructed in a several steps. First, P(PGK1) was subcloned into pNTI742. This plasmid was then linearized with SpeI and gel extracted. P(HIS4) was PCR amplified from yeast genomic DNA with primers RM739 and RM740 and mCherry was PCR amplified from a subcloned plasmid template using RM741 and RM742. The three resulting fragments were Gibson assembled.

pNTI754 through pNTI756 were cloned using a similar method, by first digesting pNTI753 with SpeI and BamHI and gel extracting the 7-kb backbone fragment. The following promoters were then amplified from yeast genomic DNA as follows: (i) P(MET6) with RM745 and RM746; (ii) P(CWP1) with RM747 and RM748; and (iii) P(PHO5) with RM749 and RM750. Each PCR-amplified promoter was then assembled into the linearized backbone by Gibson assembly.

pNTI757 through pNTI760 were all cloned using a similar method, by first PCR amplifying respective divergent promoters using the following combinations of PCR template primers: (i) pNTI753 with RM789 and RM 790; (ii) pNTI754 with RM793 and RM794; (iii) pNTI755 with RM795 and RM796; and (iv) pNTI756 with RM797 and RM798. Respective PCR products were then TOPO cloned using the TOPO Blunt system (Thermo Fisher Scientific #451245) according to manufacturer protocol.

Plasmid library construction

All pooled plasmid libraries were constructed by Gibson-style assembly using HiFi DNA assembly master mix (NEB E2621L) and transformed using either ElectroMAX DH10B (ThermoFisher #18290015) or NEB 10-beta Competent Escherichia coli (NEB #C3019H) according to manufacturer protocol. All column purifications were performed using Zymo DNA Clean and Concentrator-5 (Zymo #D4013). Dilutions of reach transformation were plated to estimate library size and ensure sufficiency library diversity. Plasmid libraries were harvested from liquid culture using the Monarch Plasmid DNA Miniprep Kit (NEB #T1010). Miniprep kit reagents were scaled to accommodate one spin column for every 5 ml of culture.

To generate estradiol-inducible barcode-expressed plasmid libraries (fig. S1), pNTI726 and pNTI728 were first digested with BamHI. Five barcodes were generated by annealing primer RM396 with one of five barcode primers,

RM391, RM392, RM393, RM394, or RM399, and extending the annealed duplex using Q5 polymerase. Four of these barcodes were inserted by Gibson assembly into BamHI-linearized pNTI726 and the last barcode DNA fragment inserted into BamHI-linearized pNTI728. Gibson reactions were purified and concentrated, transformed into ElectroMAX DH10B cells, and inoculated directly into 200 ml of lysogeny broth (LB)–carbenicillin media. Pooled libraries were harvested when batch liquid culture reached an optical density (OD) of 4.

To generate gRNA plasmid libraries, 100 pg of CRISPRi gRNA oligonucleotide library was amplified by PCR using Q5 polymerase using primers NM636 and NM637 (16). pNTI742 was digested with AvrII and the amplified guide fragments were introduced into the digested vector by Gibson assembly. The assembly product was purified and transformed into ElectroMAX DH10B cells by electroporation. Electroporated cells were inoculated directly into 500 ml of LB-carbenicillin media and harvested at an OD of 2. Serial dilutions of the initial transformation were plated to ensure sufficient library diversity (>50× coverage of 60,000 guides). Plasmid library was purified using NEB miniprep kit and pooled library was analyzed by Sanger sequencing.

Barcodes were then added to the gRNA plasmid library, targeting an average of four barcodes per gRNA (240,000 barcodes in total). First, barcode DNA fragments were generated by annealing oligos RM504 and RM505 and extending the duplex using Q5 polymerase. The following thermocycler conditions were used to avoid amplification of any specific barcode sequence. Initial denaturation at 98°C for 45 s, six cycles of annealing and extension at 68°C for 15 s and 72°C for 5 s, respectively, and finally a 12°C hold. The barcode fragments were digested with BamHI and MfeI to eliminate barcode fragments that contain these restriction sites and then purified using a DNA Clean and Concentrator-5. The library of gRNA-expressing plasmids was then digested with AflII and the barcode DNA fragments were introduced by Gibson assembly. The assembly reaction was purified using a DNA Clean and Concentrator-5 then transformed into NEB 10-beta Competent E. coli (High Efficiency) according to manufacturer protocol. Transformation dilutions were plated to estimate total number of transformants, and in parallel inoculated at several dilutions directly into LB-carbenicillin media. Liquid culture corresponding to roughly 240,000 transformants was harvested at an OD of 2 and plasmid library was extracted using NEB miniprep kit. Reagents were scaled to accommodate one spin column for every 5 ml of culture. This barcoded gRNA library was paired-end sequenced (see Barcode to gRNA assignment section) to assign barcodes with gRNAs.

P(HIS4)-yECitrine was amplified from pNTI741 using primers RM501 and RM502, P(PGK1)-yECitrine was amplified from pNTI725 using primers RM501 and RM503, and two versions of estradiol-inducible P(Z)-mCherry with specific nucleotide identifiers were amplified with either RM522 and RM524 or RM523 and RM524. The barcoded gRNA plasmid library was digested with BamHI and the four PCR products were introduced into the digested library by Gibson assembly to create the four CiBER-seq libraries. These libraries were then transformed into ElectroMAX DH10B cells by electroporation. Electroporated cells were inoculated directly into 500 ml of LB-carbenicillin media and harvested at an OD of 2. Serial dilutions of the initial transformation were plated to ensure sufficient library diversity (>50× coverage of 60,000 guides). Plasmid library was purified using NEB miniprep kit and pooled library was analyzed by Sanger sequencing.

CiBER-seq plasmid libraries for studying P(MET6), P(CWP1), P(PHO5), and P(HIS4) regulation (Fig. 1) were constructed in a similar fashion, but with key differences. pNTI743 containing divergent terminating sequences was used as the parent vector into which the gRNA library was inserted at the AvrII restriction site. Dual barcodes were next inserted into this gRNA plasmid library by digesting the plasmid library with AscI, annealing and extending RM720 and RM721, and Gibson assembling. Finally, the divergent promoters containing P(PGK1)-citrine normalizer and P(query)-mCherry expression cassette were inserted in between the two barcodes by: (i) digesting pNTI757 through pNTI760 with BciVI and gel extracting divergent promoter template; (ii) digesting dual barcoded gRNA plasmid library with AscI which cuts in between the two barcodes; and (iii) Gibson assembling each divergent promoter into the barcoded gRNA plasmid library and separately transforming and preparing these plasmid libraries as outlined above.

Construction of yeast strains

All yeast strains were constructed by transforming PCR products or plasmids linearized by restriction enzyme digestion into yeast by standard lithium acetate transformation (65). Selected, clonal transformants were confirmed by two genotyping PCRs, using primer pairs that amplify across the junction on either side of the integration. Genotyping reactions were performed with OneTaq Hotstart Polymerase (NEB #M0481S).

Yeast strains used in this study are listed in table S3. Strains with gcn2Δ or gcn4Δ genotype were constructed by first amplifying the hygromycin resistance cassette from pNTI729 by PCR, with flanking sequence homologous to the 5′ and 3′ ends of the GCN2 or GCN4 coding sequence, using primers RM579 through

RM582 for *gcn2Δ* and primers RM583 through RM586 for *gcn4Δ*. Primers RM589 and RM590 were used to genotype the upstream junction for *gcn2Δ*, whereas RM591 and RM592 were used for the downstream junction. Primers RM593 and RM590 were used to genotype the upstream junction for *gcn4Δ*, whereas RM591 and RM594 were used for the downstream junction.

gRNA expression cassettes were integrated using vectors from the EasyClone 2.0 toolkit for yeast genomic integration (*63*). Plasmids using backbone pCfB2189 were integrated by digesting with NotI, transforming this digestion, and selecting transformants on synthetic complete drop-out (SCD) – Leu plates. Plasmids using backbone pCfB2337 were integrated by digesting with NotI, transforming this digestion, plating transformations on nonselective yeast extract peptone dextrose (YEPD) media overnight, and then replica plating on hygromycin plates. Histidine prototrophy was restored by digesting pCfB2226 with NotI, transforming into the appropriate strain, and selecting transformants on SCD – His plates. Plasmid pNTI647, expressing dCas9 and tetR, was integrated as described in (*16*). Integration of gRNA expression cassettes was validated by amplifying across the upstream junction with RM527 and RM373 and across the downstream junction with RM374 and RM528. Integration of synthetic transcription factor variants were genotyped by amplifying across the upstream junction with RM372 and RM373 and across the downstream junction with RM374 and RM375.

Media

LB media was prepared by dissolving LB medium capsules (MP Biomedicals #3002-31) in ultrapure water and sterilized by autoclaving, according to manufacturer instructions. LB media was supplemented with 50 µg/ml carbenicillin (Sigma #C1389) for antibiotic selection. YEPD was prepared by dissolving yeast extract (RPI # Y20026) and peptone (RPI #20241) in ultrapure water, sterilizing by autoclaving, then supplementing with 2% final concentration of sterilized dextrose (Fisher Chemical #D16-500). SCD media was prepared by dissolving yeast nitrogen base (BD Difco #291940), dextrose to 2% final concentration, and the appropriate drop-out mix in ultrapure water, then sterilizing by filtration. SCD – Leu drop-out media was prepared using drop-out mix synthetic minus leucine (US Biological #D9525), SCD – Ura drop-out media was prepared using drop-out mix synthetic minus uracil (US Biological #D9535).

Quantitative reverse transcription PCR (qRT-PCR)

RNA was isolated from yeast by acid phenol extraction (*66*). Reverse transcription was carried out using Protoscript II reverse transcriptase (NEB #M0368L) with oligo-dT priming according to manufacturer instructions. qRT-PCR was car-

ried out using DyNAmo qPCR mastermix (ThermoFisher #F410L) according to manufacturer protocols, using a CFX96 Touch Real-Time PCR Detection System. Primers, provided in table S4, were designed using Primer Blast and validated by using a cDNA dilution standard curve. Oligonucleotide sequence for RT-PCR are listed in table S5.

Fluorescence measurements

Expression of yECitrine, under the control of the ZEM transcription factor, (Fig. 1) was monitored using a 96-well plate reader (Tecan SPARK Multimode Microplate Reader). Overnight cultures were back-diluted in 96-well round bottom plates to OD 0.05 in SCD – Ura selective media containing beta-estradiol and/or anhydrotetracycline as indicated. Fluorescence (excitation at 516 nm and emission at 540 nm) and OD_{600} were measured in triplicate every 15 min.

Turbidostat continuous culture

Yeast populations transformed with plasmid libraries were inoculated into a custom turbidostat (*67*) and maintained in SCD – Ura media at a density corresponding to an optical density 600 nm (OD_{600}) of roughly 0.8. When growth rate reached a steady state (corresponding to a doubling time of roughly 90 min), a 50-ml preinduction sample was collected. gRNA expression was then induced by injecting concentrated anyhydrotetracycline into both the growth chamber and turbidostat media reservoir to obtain a final concentration of 250 ng/ml of anyhydrotetracycline. Six doublings later (9 hours) a 50-ml postinduction sample was collected. For 3AT treatment, samples were induced by injecting concentrated 3AT into both the growth chamber and turbidostat media reservoir to obtain a final concentration of 90 mM 3AT. Two hours later, a postinduction sample was collected. For CiBER-seq experiments involving the ZEM transcription factor, media was supplemented with 8 nM beta-estradiol throughout the course of the experiment. Collected samples were pelleted by centrifugation at 4000 × *g* for 5 min, the media was aspirated, and the pellets were stored at –80°C.

Barcode sequencing

All PCR reactions were performed using Q5 polymerase (NEB M0491S) according to manufacturer protocols. PCR cycle numbers were adjusted as needed (between 6 and 12 cycles) to obtain adequate concentration of product for sequencing while avoiding overamplification. DNA was purified using DNA Clean & Concentrator (Zymo #D4013) according to the manufacturer instructions. When necessary, AMPure XP beads (Beckman Coulter #A63881) were used to purify full-length DNA product. Size distributions and concentrations of the sequencing libraries were measured before

sequencing using an Agilent TapeStation 2200 and High Sensitivity D1000 ScreenTape. To ensure proper clustering on the Illumina HiSeq4000, CiBER-seq libraries were either pooled with RNA sequencing libraries and standard 2% PhiX, or individually with 10% PhiX. PCR products were pooled and sequenced on HISeq4000 SR50 (Vincent J. Coates sequencing facility). Adapter sequences for each library are listed in table S6, and sequencing data accession numbers are available in table S7.

DNA library preparation

Plasmid DNA was extracted from yeast pellets using Zymo yeast miniprep kit (Zymo #D2004) according to manufacturer protocol, except as described below. Reagent volumes were scaled to accommodate roughly 250 million cells, as yeast pellets included 25 OD_{600} ml of yeast. Zymolyase concentration was increased to 1 µl for every 10 million cells and the digestion time was doubled to ensure complete cell wall digestion.

Extracted barcode expression plasmid libraries derived from pNTI726 and pNTI728 backbones (Fig. 1) were prepared by PCR amplification of barcode sequences with primers that incorporated flanking TruSeq adapters. Barcode sequences were first amplified by PCR with RM411 and an i5 primer from NEBNext Multiplex Oligos (NEB #E7600S) for 12 cycles. PCR products were purified and concentrated using a DNA Clean and Concentrator-5, and then used as the template for an additional six cycles of PCR amplification with NEBNext i5 and i7 primers (NEB #E7600S).

To achieve a more linear amplification, all other CiBER-seq DNA libraries were prepared using an initial linear amplification by in vitro transcription. Extracted plasmid was linearized by restriction digestion with MfeI for P(*PGK1*) and P(*HIS4*) plasmid libraries (Figs. 2 to 4) or PvuII for P(*Z*) libraries (Figs. 5 and 6). The digestion product was purified using a DNA Clean and Concentrator-5, and used as the template for an IVT reaction using T7 HiScribe (NEB #E2040S) according to the manufacturer protocol for short transcripts, with an overnight incubation at 37°C. The reaction was then treated with DNase I to remove template DNA and RNA product was purified using an RNA Clean and Concentrator-5 (Zymo #R1016). Purified RNA was used as the template for reverse transcription using ProtoScript II according to manufacturer protocol, using sequence-specific primer RM511 for P(*PGK1*) and P(*HIS4*) plasmid libraries (Figs. 2 to 4) or RM546 for P(*Z*) libraries (Figs. 5 and 6). Reverse transcription cDNA product was treated for 30 min with 0.5 µl RNASe A (ThermoFisher #EN0531) and 0.5 µl RNASe H (NEB #M0297S) to remove RNA, and then DNA was purified using a DNA Clean and Concentrator-5 column. The sequence-specific

reverse transcription primers RM511 and RM546 incorporate the i7 priming site, and the i5 priming site is included in the plasmid. The final library was generated using eight cycles of PCR amplification using NEBNext i5 and i7 dual index primers, and purified cDNA product as template. The resulting product was purified using a DNA Clean and Concentrator-5 and submitted for Illumina high-throughput sequencing.

RNA library preparation

Total RNA was harvested from yeast pellets as described above for quantitative PCR (qPCR) analysis. Extracted RNA from libraries using the pNTI726 or pNTI728 backbones (Fig. 1) was used as the template for reverse transcription by ProtoScript II using sequence-specific primer RM411, according to the manufacturer instructions. Reverse transcription product was purified using a DNA Clean and Concentrator-5 and used as the template for PCR amplification using i5 and i7 dual indexing primers (NEB #E7600S).

In CiBER-seq libraries, the barcode is present in the opposite orientation. Reverse transcription was carried out using ProtoScript II according to the manufacturer protocol for oligo-dT priming. Reverse transcription product was treated with 0.5 µl of RNAse A and 0.5 µl of RNAse H for 30 min to remove RNA, and the DNA product was purified using a DNA Clean and Concentrator-5. The resulting cDNA product was first amplified by PCR for six cycles using primers RM511 and RM512 for isolated P($HIS4$) and P($PGK1$) libraries, or primers RM512 and RM546 for P(Z) libraries, primers RM511 and RM810 for P($PGK1$) in dual barcoded CiBER-seq, and primers RM810 and RM812 for P($query$) in dual barcoded CiBER-seq. The PCR products were then purified and subsequently amplified in eight cycles of PCR using NEBNext i5 and i7 dual indexing primers. PCR products were purified using a DNA Clean and Concentrator-5 and submitted for Illumina high-throughput sequencing.

Barcode to gRNA assignment

The sequencing library for paired-end barcode-to-gRNA assignment sequencing was constructed by PCR amplification from the barcoded gRNA library using primers RM506 and RM509 for six cycles using Q5 polymerase according to the manufacturer instructions. The resulting PCR product was purified using a DNA Clean and Concentrator-5 and then used as a template for a second, 15-cycle PCR using NEBNext i5 and i7 dual indexing primers. The PCR product was purified using a DNA Clean and Concentrator-5 and analyzed using an Agilent TapeStation 2200 and High Sensitivity D1000 ScreenTape. The PCR product library was then sequenced using 150 + 150 base paired–end sequencing on an Illumina MiSeq. Barcode to gRNA as-

signment sequencing data are available under accession SRR10327353.

The PacBio sequencing library for dual barcodes to gRNA assignment was prepared without PCR amplification to avoid sequencing errors associated with the rolling circle polymerase and to maintain sequence diversity. First, 5 µg of dual barcoded gRNA plasmid library was digested with HindIII and PmeI and another 5 µg digested with BglII and XhoI. The ~1200-bp fragment for each digestion, containing dual barcode and gRNA were gel extracted and prepared for sequencing according to SMRTbell Express Template Prep Kit 2.0 (#100-938-900) according to manufacturer instructions.

Single gRNA induction

Yeast strains expressing individual gRNAs were grown overnight in YEPD, then diluted to OD$_{600}$ of 0.01 in − Leu media containing either 250 ng/ml anhydrotetracycline, or no inducer. Yeast were harvested 12 hours later (after roughly 6 doublings), pelleted at $4000 \times g$ for 5 min, and pellets were frozen and stored at −80°C for subsequent RNA extraction or protein isolation.

Immunoblotting

Total protein was isolated from frozen yeast pellets by resuspending in 1.5 ml of 5% trichloroacetic acid and incubated at 4°C for <10 min. Protein was pelleted by centrifugation at $16,000 \times g$ for 2 min and washed in 0.5 ml of acetone, vortexed briefly, and collected by centrifugation for 5 min at $16,000 \times g$. Protein pellets were washed once more in 1 ml of acetone, vortexed, and collected by centrifugation for 5 min at $16,000 \times g$. Pellets were dried overnight and then resuspended in 100 µl of freshly prepared protein breakage buffer [50 mM Tris•HCl pH 7.5, 1 mM EDTA, and 3 mM dithiothreitol (DTT)] containing 100 µl of glass beads (BioSpec 11079105). Samples were vortexed in five cycles of 1-min vortexing followed by 1 min on ice. Lysates were transferred to new tubes and collected by centrifugation at $16,000 \times g$, then resuspended in 150 µl resuspension buffer (100 mM Tris•HCl pH 11, 3% SDS). Samples were boiled for 5 min then allowed to cool and pelleted at $16,000 \times g$ for 30 s. Then, 120 µl of lysate was transferred to a new tube, and a bicinchoninic acid (BCA) assay was performed to determine protein abundance. Equal amounts of total protein were loaded on a 4 to 12% polyacrylamide Bis-Tris gel (Thermo Scientific #NW04120BOX) and separated by electrophoresis in MOPS buffer at 200 V in a Bolt gel tank (Thermo Scientific #A25977) according to manufacturer instructions. Protein was then transferred to a nitrocellulose membrane (Thermo Scientific #88018) according to manufacturer guidelines. Membranes were blocked for 1 hour in tris-

buffered saline with Tween 20 (TBST) with 5% milk, washed with TBST three times for 10 min of shaking, and incubated with primary antibodies in TBST plus 0.5% milk overnight. Hexokinase loading control was probed with rabbit anti-Hxk2 (Rockland #100-4159) and phosphorylated eIF2α was detected using Phospho-eIF2a (Ser52) Polyclonal Antibody (Invitrogen #44-728G). Membranes were then washed and probed with secondary antibody anti-rabbit immunoglobulin G (IgG), HRP-linked antibody (Cell Signaling Technology #7074S). Membrane was imaged by Pierce enhanced chemiluminesence (ECL) Western blotting substrate (ThermoScientific #32209) and the chemiluminescence measured on a FluorChem R (ProteinSimple).

Sequencing data analysis

Analysis software is archived (68). Sequencing data were processed using Cutadapt to remove constant adapter sequences and demultiplex libraries based on embedded nucleotide identifiers. The adapter sequences for each experimental dataset are provided in table S6. The underlined sequence represents the library-specific nucleotide identifier.

For dual-guide experiments (Fig. 4), demultiplexing was not required as each pool derived from a single P($HIS4$) library. For this reason, adapter trimming was performed by instead taking the first 25 nucleotides using fastx_trimmer.

Trimmed barcodes were then counted using the custom "bc-seqs" program, which collapses barcode variants separated by single-nucleotide mismatches (16). Using the "bc-tabulate" script, these barcode counts were then collected into a matrix, tabulating samples within an experiment. The P($HIS4$) and P($PGK1$) libraries were sequenced in two Illumina HiSeq4000 runs and the barcode counts for the runs were summed.

Barcodes were first filtered to remove those that lacked at least 32 counts for at least one replicate in the preinduction DNA sample, or the preinduction P($PGK1$)-normalizing sample for dual-barcoded experiments. The remaining barcodes were evaluated by differential activity analysis using mpralm (18). Barcode expression was compared between samples before and after gRNA induction or before and after 3AT treatment. Analysis was performed using the aggregate = "sum" parameter to sum barcodes that corresponded to the same gRNA and model_type = "indep_groups," which treats the replicates as independent experiments. Output tables were merged with gene information from the *Saccharomyces* Genome Database. Scatterplots comparing log fold change values of individual gRNAs showing were first thresholded for guides in which $q < 0.05$ in at least one of the two expression analyses. Barcodes corresponding to no-guide

plasmids were used as negative controls to determine the distribution of P values. Genes involved in amino acid biosynthesis, aminoacyl tRNA charging, ISR-controlled translation initiation, RNA polymerase III transcription, tRNA processing, or actin cytoskeletal arrangement were hand-curated and used to annotate volcano and scatter plots.

REFERENCES AND NOTES

1. G. J. Knott, J. A. Doudna, CRISPR-Cas guides the future of genetic engineering. *Science* **361**, 866–869 (2018). doi: 10.1126/science.aat5011; pmid: 30166482
2. L. Cong et al., Multiplex genome engineering using CRISPR/Cas systems. *Science* **339**, 819–823 (2013). doi: 10.1126/science.1231143; pmid: 23287718
3. M. Jinek et al., RNA-programmed genome editing in human cells. *eLife* **2**, e00471 (2013). doi: 10.7554/eLife.00471; pmid: 23386978
4. P. Mali et al., RNA-guided human genome engineering via Cas9. *Science* **339**, 823–826 (2013). doi: 10.1126/science.1232033; pmid: 23287722
5. L. A. Gilbert et al., CRISPR-mediated modular RNA-guided regulation of transcription in eukaryotes. *Cell* **154**, 442–451 (2013). doi: 10.1016/j.cell.2013.06.044; pmid: 23849981
6. H. Koike-Yusa, Y. Li, E.-P. Tan, M. D. C. Velasco-Herrera, K. Yusa, Genome-wide recessive genetic screening in mammalian cells with a lentiviral CRISPR-guide RNA library. *Nat. Biotechnol.* **32**, 267–273 (2014). doi: 10.1038/nbt.2800; pmid: 24535568
7. O. Shalem et al., Genome-scale CRISPR-Cas9 knockout screening in human cells. *Science* **343**, 84–87 (2014). doi: 10.1126/science.1247005; pmid: 24336571
8. T. Wang, J. J. Wei, D. M. Sabatini, E. S. Lander, Genetic screens in human cells using the CRISPR-Cas9 system. *Science* **343**, 80–84 (2014). doi: 10.1126/science.1246981; pmid: 24336569
9. M. Kampmann, CRISPRi and CRISPRa Screens in Mammalian Cells for Precision Biology and Medicine. *ACS Chem. Biol.* **13**, 406–416 (2018). doi: 10.1021/acschembio.7b00657; pmid: 29035510
10. R. P. Patwardhan et al., High-resolution analysis of DNA regulatory elements by synthetic saturation mutagenesis. *Nat. Biotechnol.* **27**, 1173–1175 (2009). doi: 10.1038/nbt.1589; pmid: 19915551
11. M. Breker, M. Schuldiner, Explorations in topology-delving underneath the surface of genetic interaction maps. *Mol. Biosyst.* **5**, 1473–1481 (2009). doi: 10.1039/b907076c; pmid: 19763324
12. B. Adamson et al., A Multiplexed Single-Cell CRISPR Screening Platform Enables Systematic Dissection of the Unfolded Protein Response. *Cell* **167**, 1867–1882.e21 (2016). doi: 10.1016/j.cell.2016.11.048; pmid: 27984733
13. A. Dixit et al., Perturb-Seq: Dissecting Molecular Circuits with Scalable Single-Cell RNA Profiling of Pooled Genetic Screens. *Cell* **167**, 1853–1866.e17 (2016). doi: 10.1016/j.cell.2016.11.038; pmid: 27984732
14. D. A. Jaitin et al., Dissecting Immune Circuits by Linking CRISPR-Pooled Screens with Single-Cell RNA-Seq. *Cell* **167**, 1883–1896.e15 (2016). doi: 10.1016/j.cell.2016.11.039; pmid: 27984734
15. P. Datlinger et al., Pooled CRISPR screening with single-cell transcriptome readout. *Nat. Methods* **14**, 297–301 (2017). doi: 10.1038/nmeth.4177; pmid: 28099430
16. N. J. McGlincy et al., A genome-scale CRISPR interference guide library enables comprehensive phenotypic profiling in yeast. *bioRxiv* 2020.03.11.988105 [Preprint]. 12 March 2020. doi: 10.1101/2020.03.11.988105
17. J. D. Smith et al., Quantitative CRISPR interference screens in yeast identify chemical-genetic interactions and new rules for guide RNA design. *Genome Biol.* **17**, 45 (2016). doi: 10.1186/s13059-016-0900-9; pmid: 26956608
18. L. Myint, D. G. Avramopoulos, L. A. Goff, K. D. Hansen, Linear models enable powerful differential activity analysis in massively parallel reporter assays. *BMC Genomics* **20**, 209 (2019). doi: 10.1186/s12864-019-5556-x; pmid: 30866806
19. M. E. Ritchie et al., limma powers differential expression analyses for RNA-sequencing and microarray studies. *Nucleic Acids Res.* **43**, e47 (2015). doi: 10.1093/nar/gkv007; pmid: 25605792
20. P. Kaiser, K. Flick, C. Wittenberg, S. I. Reed, Regulation of transcription by ubiquitination without proteolysis: Cdc34/SCF^Met30-mediated inactivation of the transcription factor Met4. *Cell* **102**, 303–314 (2000). doi: 10.1016/S0092-8674(00)00036-2; pmid: 10975521
21. G. J. Smits, L. R. Schenkman, S. Brul, J. R. Pringle, F. M. Klis, Role of cell cycle-regulated expression in the localized incorporation of cell wall proteins in yeast. *Mol. Biol. Cell* **17**, 3267–3280 (2006). doi: 10.1091/mbc.e05-08-0738; pmid: 16672383
22. Y. P. Bhavsar-Jog, E. Bi, Mechanics and regulation of cytokinesis in budding yeast. *Semin. Cell Dev. Biol.* **66**, 107–118 (2017). doi: 10.1016/j.semcdb.2016.12.010; pmid: 28034796
23. P. Korber, S. Barbaric, The yeast PHO5 promoter: From single locus to systems biology of a paradigm for gene regulation through chromatin. *Nucleic Acids Res.* **42**, 10888–10902 (2014). doi: 10.1093/nar/gku784; pmid: 25190457
24. A. G. Hinnebusch, Translational regulation of GCN4 and the general amino acid control of yeast. *Annu. Rev. Microbiol.* **59**, 407–450 (2005). doi: 10.1146/annurev.micro.59.031805.133833; pmid: 16153175
25. A. Chambers, E. A. Packham, I. R. Graham, Control of glycolytic gene expression in the budding yeast (*Saccharomyces cerevisiae*). *Curr. Genet.* **29**, 1–9 (1995). doi: 10.1007/BF00313187; pmid: 8595651
26. P. K. Maitra, Z. Lobo, Control of glycolytic enzyme synthesis in yeast by products of the hexokinase reaction. *J. Biol. Chem.* **246**, 489–499 (1971). pmid: 4250748
27. N. P. Williams, A. G. Hinnebusch, T. F. Donahue, Mutations in the structural genes for eukaryotic initiation factors 2 alpha and 2 beta of *Saccharomyces cerevisiae* disrupt translational control of GCN4 mRNA. *Proc. Natl. Acad. Sci. U.S.A.* **86**, 7515–7519 (1989). doi: 10.1073/pnas.86.19.7515; pmid: 2678106
28. A. K. Hopper, Transfer RNA post-transcriptional processing, turnover, and subcellular dynamics in the yeast *Saccharomyces cerevisiae*. *Genetics* **194**, 43–67 (2013). doi: 10.1534/genetics.112.147470; pmid: 23633143
29. T. E. Dever, W. Yang, S. Åström, A. S. Byström, A. G. Hinnebusch, Modulation of tRNA(iMet), eIF-2, and eIF-2B expression shows that GCN4 translation is inversely coupled to the level of eIF-2.GTP.Met-tRNA(iMet) ternary complexes. *Mol. Cell. Biol.* **15**, 6351–6363 (1995). doi: 10.1128/MCB.15.11.6351; pmid: 7565788
30. C. Conesa et al., Modulation of yeast genome expression in response to defective RNA polymerase III-dependent transcription. *Mol. Cell. Biol.* **25**, 8631–8642 (2005). doi: 10.1128/MCB.25.19.8631-8642.2005; pmid: 16166643
31. R. Shemer, A. Meimoun, T. Holtzman, D. Kornitzer, Regulation of the transcription factor Gcn4 by Pho85 cyclin PCL5. *Mol. Cell. Biol.* **22**, 5395–5404 (2002). doi: 10.1128/MCB.22.15.5395-5404.2002; pmid: 12101234
32. R. C. Wek, H. Y. Jiang, T. G. Anthony, Coping with stress: eIF2 kinases and translational control. *Biochem. Soc. Trans.* **34**, 7–11 (2006). doi: 10.1042/BST0340007; pmid: 16246168
33. N. S. Bae, A. P. Seberg, L. P. Carroll, M. J. Swanson, Identification of Genes in *Saccharomyces cerevisiae* that Are Haploinsufficient for Overcoming Amino Acid Starvation. *G3* **7**, 1061–1084 (2017). doi: 10.1534/g3.116.037416; pmid: 28209762
34. H. Kubota, Y. Sakaki, T. Ito, GI domain-mediated association of the eukaryotic initiation factor 2α kinase GCN2 with its activator GCN1 is required for general amino acid control in budding yeast. *J. Biol. Chem.* **275**, 20243–20246 (2000). doi: 10.1074/jbc.C000262200; pmid: 10801780
35. E. Sattlegger et al., YIH1 is an actin-binding protein that inhibits protein kinase GCN2 and impairs general amino acid control when overexpressed. *J. Biol. Chem.* **279**, 29952–29962 (2004). doi: 10.1074/jbc.M404009200; pmid: 15126500
36. I. A. Olave, S. L. Reck-Peterson, G. R. Crabtree, Nuclear actin and actin-related proteins in chromatin remodeling. *Annu. Rev. Biochem.* **71**, 755–781 (2002). doi: 10.1146/annurev.biochem.71.110601.135507; pmid: 12045110
37. D. Kornitzer, B. Raboy, R. G. Kulka, G. R. Fink, Regulated degradation of the transcription factor Gcn4. *EMBO J.* **13**, 6021–6030 (1994). doi: 10.1002/j.1460-2075.1994.tb06948.x; pmid: 7813440
38. E. S. Johnson, Protein modification by SUMO. *Annu. Rev. Biochem.* **73**, 355–382 (2004). doi: 10.1146/annurev.biochem.73.011303.074118; pmid: 15189146
39. A. Hoelz, E. W. Debler, G. Blobel, The structure of the nuclear pore complex. *Annu. Rev. Biochem.* **80**, 613–643 (2011). doi: 10.1146/annurev-biochem-060109-151030; pmid: 21495847
40. E. Rosonina, S. M. Duncan, J. L. Manley, Sumoylation of transcription factor Gcn4 facilitates its Srb10-mediated clearance from promoters in yeast. *Genes Dev.* **26**, 350–355 (2012). doi: 10.1101/gad.184689.111; pmid: 22345516
41. A. Akhter, E. Rosonina, Chromatin Association of Gcn4 Is Limited by Post-translational Modifications Triggered by its DNA-Binding in *Saccharomyces cerevisiae*. *Genetics* **204**, 1433–1445 (2016). doi: 10.1534/genetics.116.194134; pmid: 27770033
42. S. J. Li, M. Hochstrasser, A new protease required for cell-cycle progression in yeast. *Nature* **398**, 246–251 (1999). doi: 10.1038/18457; pmid: 10094048
43. S. J. Li, M. Hochstrasser, The Ulp1 SUMO isopeptidase: Distinct domains required for viability, nuclear envelope localization, and substrate specificity. *J. Cell Biol.* **160**, 1069–1082 (2003). doi: 10.1083/jcb.200212052; pmid: 12654900
44. V. G. Panse, B. Küster, T. Gerstberger, E. Hurt, Unconventional tethering of Ulp1 to the transport channel of the nuclear pore complex by karyopherins. *Nat. Cell Biol.* **5**, 21–27 (2003). doi: 10.1038/ncb893; pmid: 12471376
45. B. Palancade et al., Nucleoporins prevent DNA damage accumulation by modulating Ulp1-dependent sumoylation processes. *Mol. Biol. Cell* **18**, 2912–2923 (2007). doi: 10.1091/mbc.e07-02-0123; pmid: 17538013
46. J. O. Rouvière et al., A SUMO-dependent feedback loop senses and controls the biogenesis of nuclear pore subunits. *Nat. Commun.* **9**, 1665 (2018). doi: 10.1038/s41467-018-03673-3; pmid: 29695777
47. L. Texari et al., The nuclear pore regulates GAL1 gene transcription by controlling the localization of the SUMO protease Ulp1. *Mol. Cell* **51**, 807–818 (2013). doi: 10.1016/j.molcel.2013.08.047; pmid: 24074957
48. G. Albrecht, H. U. Mösch, B. Hoffmann, U. Reusser, G. H. Braus, Monitoring the Gcn4 protein-mediated response in the yeast *Saccharomyces cerevisiae*. *J. Biol. Chem.* **273**, 12696–12702 (1998). doi: 10.1074/jbc.273.21.12696; pmid: 9582292
49. A. M. Darnell, A. R. Subramaniam, E. K. O'Shea, Translational Control through Differential Ribosome Pausing during Amino Acid Limitation in Mammalian Cells. *Mol. Cell* **71**, 229–243.e11 (2018). doi: 10.1016/j.molcel.2018.06.041; pmid: 30029003
50. M. R. McFarland et al., The molecular aetiology of tRNA synthetase depletion: Induction of a GCN4 amino acid starvation response despite homeostatic maintenance of charged tRNA levels. *Nucleic Acids Res.* **48**, 3071–3088 (2020). doi: 10.1093/nar/gkaa055; pmid: 32016368
51. H. Qiu et al., Defects in tRNA processing and nuclear export induce GCN4 translation independently of phosphorylation of the alpha subunit of eukaryotic translation initiation factor 2. *Mol. Cell. Biol.* **20**, 2505–2516 (2000). doi: 10.1128/MCB.20.7.2505-2516.2000; pmid: 10713174
52. S. Kirchner, Z. Ignatova, Emerging roles of tRNA in adaptive translation, signalling dynamics and disease. *Nat. Rev. Genet.* **16**, 98–112 (2015). doi: 10.1038/nrg3861; pmid: 25534324
53. S. R. Lee, K. Collins, Starvation-induced cleavage of the tRNA anticodon loop in Tetrahymena thermophila. *J. Biol. Chem.* **280**, 42744–42749 (2005). doi: 10.1074/jbc.M510356200; pmid: 16272149
54. D. M. Thompson, C. Lu, P. J. Green, R. Parker, tRNA cleavage is a conserved response to oxidative stress in eukaryotes. *RNA* **14**, 2095–2103 (2008). doi: 10.1261/rna.1232808; pmid: 18719243
55. S. Yamasaki, P. Ivanov, G. F. Hu, P. Anderson, Angiogenin cleaves tRNA and promotes stress-induced translational repression. *J. Cell Biol.* **185**, 35–42 (2009). doi: 10.1083/jcb.200811106; pmid: 19332886
56. D. Huh et al., An adaptive stress-induced tRNA depletion response mediates codon-based gene repression and growth suppression. *bioRxiv* 416727 [Preprint]. 13 September 2018. doi: 10.1101/416727
57. M. Kapur, C. E. Monaghan, S. L. Ackerman, Regulation of mRNA Translation in Neurons-A Matter of Life and Death. *Neuron* **96**, 616–637 (2017). doi: 10.1016/j.neuron.2017.09.057; pmid: 29096076
58. R. Ishimura et al., Ribosome stalling induced by mutation of a CNS-specific tRNA causes neurodegeneration. *Science* **345**, 455–459 (2014). doi: 10.1126/science.1249749; pmid: 25061210
59. R. Ishimura, G. Nagy, I. Dotu, J. H. Chuang, S. L. Ackerman, Activation of GCN2 kinase by ribosome stalling links translation elongation with translation initiation. *eLife* **5**, e14295 (2016). doi: 10.7554/eLife.14295; pmid: 27085088
60. B. D. Alford, G. Valiant, O. Brandman, Genome-wide, time-sensitive interrogation of the heat shock response under

diverse stressors via ReporterSeq. bioRxiv 2020.03.29.014845 [Preprint]. 31 March 2020. .doi: 10.1101/2020.03.29.014845

61. M. A. Sheff, K. S. Thorn, Optimized cassettes for fluorescent protein tagging in *Saccharomyces cerevisiae*. *Yeast* **21**, 661–670 (2004). doi: 10.1002/yea.1130; pmid: 15197731

62. A. Aranda-Díaz, K. Mace, I. Zuleta, P. Harrigan, H. El-Samad, Robust Synthetic Circuits for Two-Dimensional Control of Gene Expression in Yeast. *ACS Synth. Biol.* **6**, 545–554 (2017). doi: 10.1021/acssynbio.6b00251; pmid: 27930885

63. V. Stovicek, G. M. Borja, J. Forster, I. Borodina, EasyClone 2.0: Expanded toolkit of integrative vectors for stable gene expression in industrial *Saccharomyces cerevisiae* strains. *J. Ind. Microbiol. Biotechnol.* **42**, 1519–1531 (2015). doi: 10.1007/s10295-015-1684-8; pmid: 26376869

64. T. W. Christianson, R. S. Sikorski, M. Dante, J. H. Shero, P. Hieter, Multifunctional yeast high-copy-number shuttle vectors. *Gene* **110**, 119–122 (1992). doi: 10.1016/0378-1119(92)90454-W; pmid: 1544568

65. R. D. Gietz, R. H. Schiestl, High-efficiency yeast transformation using the LiAc/SS carrier DNA/PEG method. *Nat. Protoc.* **2**, 31–34 (2007). doi: 10.1038/nprot.2007.13; pmid: 17401334

66. M. Ares, Isolation of total RNA from yeast cell cultures. *Cold Spring Harb. Protoc.* **2012**, 1082–1086 (2012). doi: 10.1101/pdb.prot071456; pmid: 23028070

67. A. M. McGeachy, Z. A. Meacham, N. T. Ingolia, An Accessible Continuous-Culture Turbidostat for Pooled Analysis of Complex Libraries. *ACS Synth. Biol.* **8**, 844–856 (2019). doi: 10.1021/acssynbio.8b00529; pmid: 30908907

68. R. Muller, Z. A. Meacham, L. Ferguson, N. T. Ingolia, CiBER-seq dissects genetic networks by quantitative CRISPRi profiling of expression phenotypes, version 1, Zenodo (2020); doi: 10.5281/zenodo.4035711

SUPPLEMENTARY MATERIALS

science.sciencemag.org/content/370/6522/eabb9662/suppl/DC1
Figs. S1 to S6
Tables S1 to S7
MDAR Reproducibility Checklist
Data S1

View/request a protocol for this paper from *Bio-protocol*.

Science

CiBER-seq dissects genetic networks by quantitative CRISPRi profiling of expression phenotypes

Ryan Muller, Zuriah A. Meacham, Lucas Ferguson and Nicholas T. Ingolia

CiBER-seq dissects genetic networks

Cells integrate environmental signals and internal states to dynamically control gene expression. Muller *et al.* developed a technique to dissect this cellular logic by linking targeted, genome-wide genetic perturbations with a deep-sequencing readout that quantitatively measured the expression phenotype induced by each perturbation. The method, dubbed CiBER-seq, was able to recapitulate known regulatory pathways linking protein synthesis with nutrient availability in budding yeast cells. Unexpectedly, the authors found that the cellular logic also appears to consider protein production machinery in this decision. By uncovering additional facets of this deeply conserved pathway, the findings demonstrate the utility of comprehensive and quantitative CiBER-seq profiling in mapping the gene networks underlying cellular decisions.

Science, this issue p. eabb9662

ARTICLE TOOLS	http://science.sciencemag.org/content/370/6522/eabb9662
SUPPLEMENTARY MATERIALS	http://science.sciencemag.org/content/suppl/2020/12/09/370.6522.eabb9662.DC1
REFERENCES	This article cites 67 articles, 29 of which you can access for free http://science.sciencemag.org/content/370/6522/eabb9662#BIBL
PERMISSIONS	http://www.sciencemag.org/help/reprints-and-permissions

Use of this article is subject to the Terms of Service